INTERACTION OF CO_2 LASER LIGHT WITH A DENSE Z-PINCH PLASMA

by

GEORG F. ALBRECHT

Dipl. Phys, U. of Stuttgart, 1974

A THESIS SUBMITTED IN PARTIAL FULFILLMENT OF

THE REQUIREMENTS FOR THE DEGREE OF

DOCTOR OF PHILOSOPHY

in

THE FACULTY OF GRADUATE STUDIES

Department of Physics

We accept this thesis as conforming

to the required standard

THE UNIVERSITY OF BRITISH COLUMBIA

May, 1979

In presenting this thesis in partial fulfilment of the requirements for an advanced degree at the University of British Columbia, I agree that the Library shall make it freely available for reference and study. I further agree that permission for extensive copying of this thesis for scholarly purposes may be granted by the Head of my Department or by his representatives. It is understood that copying or publication of this thesis for financial gain shall not be allowed without my written permission.

Department of ~~Physics, Plasma Physics~~ Physics

The University of British Columbia
2075 Wesbrook Place
Vancouver, Canada
V6T 1W5

Date May 25th 1979

Research Supervisor: J. Meyer

Abstract

The interaction of a 250 MW CO_2 laser pulse with a Z-pinch plasma has been observed. Heating by inverse bremsstrahlung and stimulated Brillouin scattering off a plasma with a few times $10^{17}\ \frac{\text{electrons}}{\text{cm}^3}$, $T_e \sim 150$ eV and temperature scale lengths of a few mm is shown to occur. The observed angular dependence of the Brillouin backscattered light is in good agreement with current theories. Some of the backscattered light shows intensity modulations at the electron gyro frequency.

Finally, the successful nano second gating of an Optical Multichannel Analyser is described and applied to spectroscopical density measurements of the plasma.

TABLE OF CONTENTS

TABLE OF CONTENTS

List of Symbols

$\vec{k}$, $\vec{k}_o$, $\vec{k}_\pm$	wave vectors of the plasma density fluctuations, the incident and the scattered light waves
ω, ω_o, $\omega_\pm$	frequencies of the plasma density fluctuation, the incident and the scattered light waves
$\vec{E}_o$, $\vec{E}_\pm$	electric fields of the incident and scattered electromagnetic waves
$j_\pm$	currents in the plasma at the scattered frequencies
$\sigma_\pm$	conductivity of the plasma at the scattered frequencies
δn_{enh}	amplitude of the enhanced density fluctuation
q	electric unit charge of either ion or electron
e	electric unit charge of electron
$v_{o\pm}$	quiver velocity of an electron in the incident electromagnetic wave at frequencies $\pm\ \omega_o$
m_e	mass of the electron
M	mass of the atom (He)
$\varepsilon_\pm$	dielectric constant at $\omega_\pm$
$\chi_{e,i}$	electronic, ionic susceptibility
c	speed of light
n_o	average electron density
$\omega_{pe,i}$	plasma frequencies of electrons/ions
Ψ	ponderomotive potential
$D_\pm$	see (I-12)
ξ	high frequency coordinate of electrons oscillating in an electromagnetic field
R	coordinate along which the electric field varies

$f_{i,e}$	distribution function for ions, electrons
f_o	Maxwellian equilibrium distribution function
Φ	self-consistent potential within plasma
Γ_o, Γ_a	damping of electromagnetic wave and ion wave (Landau and collisional)
λ_D	Debye length
ϕ	angle between k and v_o (Ch. I) also angular coordinate (3.21)
γ	growth rate for a parametric decay instability
α	$\alpha = \frac{1}{k\lambda_D}$
$S(\alpha)$	Shape factor of the Thomson scattered ion feature
$T_{e,i}$	ion, electron temperature
κ_B	inverse bremsstrahlung absorption length
κ_T	thermal conductivity
k_B	Boltzmann constant
$\ln \Lambda$	Coulomb logarithm, ≈ 10
I_o, I_{inc}	laser light intensity incident on the plasma
I_{BS}	backscattered laser light intensity (thermal, enhanced, denoted by superscripts)
$\delta\theta_{BS}$, $\theta_{D\ min}$	angular divergence of backscattered light for different physical models
ℓ	length of interaction volume; scale lengths
β	inverse gain length of light amplified by SBS
v_{ia}	ion-acoustic speed
V_{LP}	laser-plasma interaction volume

to my father,

for his infinite love, trust and support.

to Marilyn,

for all she taught me.

to the pleasure of a loving woman's touch,

it is the difference between living

and vegetating.

Introduction

The current efforts in controlled thermonuclear fusion research have brought about a great interest in laser plasma interaction studies. The "inertial confinement" type of experiment attempts to achieve controlled fusion by focussing enormous laser powers (.5 peta watts) on small DT pellets (some 100μ diameter) and thus heat and compress the created plasma to temperatures and densities at which thermonuclear reactions yield more energy than was put in in form of laser energy.[1,2,3] The key questions that arise in this approach concern the coupling of laser light to the plasma, a problem of surmounting complexity. The type of experiments in which the plasma is magnetically confined attempts to achieve controlled fusion not so much by reducing the mean free path between reactions by plasma compression but by increasing the confinement time to an extent that a sufficient amount of thermonuclear energy can be released before the plasma decays. One of the most important problems in this approach is the heating of the plasma to sufficient temperatures.[5] Dawson et al.[6] suggested that high power CO_2 lasers be used to achieve significant heating of magnetically confined plasmas because these types of plasmas are in a density regime where the inverse bremsstrahlung absorption for CO_2 laser light becomes significant. A number of experiments have been performed along these lines.[5,7,8,9,28]

In either case it is of great importance to investigate laser plasma interactions under different conditions in order to learn about the possible physical processes involved and to aid theories that try to predict such processes.

The experiment described in this report was set up to investigate which laser plasma interaction processes can be studied with the means currently available in this laboratory.

Chapter I describes the basics of the theory of one of the most important types of processes happening in high power laser plasma interactions, namely the parametric decay of a light wave in plasma waves and scattered light waves. The case of stimulated Brillouin scattering is treated in some detail.

Chapter II describes the experiments performed with a 250 MW CO_2 laser and a high density Z-pinch plasma and the results that were obtained.

Chapter III discusses these results and conclusions are drawn about the occurrence of stimulated Brillouin scattering, the angular divergence of its backscattered light and the intensity modulation of some of the backscattered light with the gyro frequency of electrons. The absorption of CO_2 laser light by inverse bremsstrahlung in some experiments is verified.

Chapter IV describes a contribution to the diagnostics of the Z-pinch plasma. A new technique for satisfactory nsec gating of an Optical Multichannel Analyser is applied to spectroscopical studies of the plasma density using the 4686Å line of He II.

CHAPTER I

Theory of parametric decay in an infinite, homogeneous plasma and its application to stimulated Brillouin scattering.

1.1 Introduction

This chapter attempts to provide an easily readable presentation of the theory of parametric decay instabilities in an infinite homogeneous plasma. As it is neither supposed to be a comprehensive review nor a cumbersome reproduction of work already done,[10-15] the presentation is limited to the process most relevant for the experiment to be described later, e.g. the process of lowest threshold and high growthrate namely stimulated Brillouin scattering.

Furthermore, the emphasis will be on physical interpretation rather than the mathematical apparatus.

First, a simple picture of a parametric process shall be given. Imagine an electromagnetic wave $(\vec{k}_o, \omega_o)$ incident on a plasma with thermal density fluctuations. Let us assume that the electromagnetic wave scatters off a fourier component $(\vec{k}, \omega)$ of these density fluctuations thus creating a scattered electromagnetic wave at $\vec{k}_- = \vec{k}_o - \vec{k}$ (conservation of wave momentum) and frequency $\omega_- = \omega_o - \omega$ (conservation of energy).

In the case of small incident intensities this scattered wave will leave the plasma without perturbing it any further. With increasing incident intensities however, a situation will arise in which the intensity of the scattered light at $(\omega_-, \vec{k}_-)$ will indeed be high enough to itself affect the plasma. Now we have the new situation of two electromagnetic waves, namely one at $(\vec{k}_o, \omega_o)$ and one at $(\vec{k}_-, \omega_-)$ being simultaneously present in the plasma.

If both waves interact linearly with the plasma, nothing spectacular will happen and electrons will oscillate at frequencies ω_o and ω_-. If, however, the two waves couple to each other via the plasma, not only the frequencies at ω_o and ω_- will occur in the plasma, but also the sum and difference frequencies $\omega_o + \omega_-$ and $\omega_o - \omega_-$. It will be seen that this nonlinear coupling indeed takes place via the ponderomotive force, to be explained later. Of these two frequencies, $\omega_o + \omega_-$ and $\omega_o - \omega_-$, the low frequency at $\omega_o - \omega_-$ will couple much stronger to the plasma as the amplitude of an electron oscillating in an electromagnetic field is proportional to $\frac{1}{\omega^2}$. Therefore, the simultaneous presence of the two electromagnetic waves at $(\vec{k}_o, \omega_o)$ and $(\vec{k}_-, \omega_-)$ will set up a plasma wave at $\vec{k}_o - \vec{k}_- = \vec{k}_o - (\vec{k}_o - \vec{k}) = \vec{k}$ and $\omega_o - \omega_- = \omega_o - (\omega_o - \omega) = \omega$.
In other words, the beat of the incident and scattered electromagnetic wave in the plasma will enhance exactly that density fluctuation which initially scattered the incident electromagnetic wave.
If the plasma wave at (k, ω) is built up to an extent that thermalization cannot destroy it anymore, more light yet will be scattered at the now enhanced density fluctuation, which in turn will beat again with the incident light wave to enhance the density fluctuation even more and thus a scattering instability or "stimulated scattering" will take place.
The threshold will, as indicated, depend on how effective the beat wave is imprinted onto the plasma by the electromagnetic fields against the randomizing effects of collisional and Landau damping.
With this simple picture in mind, the theoretical model describing these parametric processes can easily be followed.

1.2 Outline of the theory

Maxwell's equations describe the generation of electromagnetic waves at frequencies $\omega_{\pm} = \omega \pm \omega_o$ due to source terms at the same frequencies. The forces in the plasma arising from the beat of the incident and the scattered light wave are best described by introducing the ponderomotive potential. Together with the self-consistent potential, calculated from Poisson's equation, it will provide the force terms in the Vlasov equation. The latter then allows density fluctuations at ω, $\vec{k}$ in the plasma due to the beat of two electromagnetic waves to be calculated.

The Vlasov equation for the density fluctuations δn and the equations for $\vec{E}_{\pm}$* form a set of coupled equations for δn and $\vec{E}_{\pm}$; the solution of this system is a dispersion relation describing the propagation of electromagnetic waves as a function of the propagation of plasma waves under various conditions. This relation makes it possible to calculate thresholds and growthrates for different types of processes.

* $\vec{E}_{\pm} = \vec{E}(\omega \pm \omega_o)$

1.3 Derivation of the general dispersion relation

As pointed out in the outline of the theory, we start out with Maxwell's equations to describe the generation of electromagnetic waves at the scattered frequencies $\omega_{\pm} = \omega \pm \omega_o$.

Eliminating $\tilde{H}_{\pm}$ out of

$$\nabla \times \tilde{E}_{\pm}^{(*)} = -\frac{1}{c}\frac{\partial \tilde{B}_{\pm}}{\partial t} \quad \text{and} \quad \nabla \times \tilde{H}_{\pm} = \frac{4\pi}{c}\tilde{j}_{\pm} + \frac{1}{c}\frac{\partial \tilde{E}_{\pm}}{\partial t} \tag{I-1}$$

where $\tilde{B} = \mu \tilde{H}$ and $\mu = 1$ (I-2)

one gets

$$\nabla \times (\nabla \times \tilde{E}_{\pm}) = -\frac{4\pi}{c^2}\frac{\partial \tilde{j}_{\pm}}{\partial t} - \frac{1}{c^2}\frac{\partial^2 \tilde{E}_{\pm}}{\partial t^2} \tag{I-3}$$

and with

$$\nabla \times (\nabla \times \tilde{E}_{\pm}) = (\text{grad div} - \Delta)\, \tilde{E}_{\pm} \tag{I-4}$$

this becomes

$$-\Delta \tilde{E}_{\pm} + \frac{1}{c^2}\frac{\partial^2 \tilde{E}_{\pm}}{\partial t^2} = -\frac{4\pi}{c^2}\frac{\partial \tilde{j}_{\pm}}{\partial t} - \text{grad div}\, \tilde{E}_{\pm} \tag{I-5}$$

The R.H.S. of equation (I-5) means that the electromagnetic wave $\tilde{E}_{\pm}$ has source terms due to currents $\tilde{j}_{\pm}$ flowing in the plasma and due to self-consistent fields which will have to be calculated using Poisson's equation.

Fourier transforming the equation (I-5) using

$$\tilde{E}(\vec{x}, t) = \frac{1}{4\pi^2}\int_{\substack{\text{all } \omega \\ \text{all } k}} E(\vec{k}, \omega)\, e^{i(\vec{k}\vec{x} - \omega t)}\, d^3k d\omega \tag{I-6}$$

(*) $\vec{E}_+ = \vec{E}(\omega_+)$
$\vec{E}_- = \vec{E}(\omega_-)$

we find

$$\left[\left(-\frac{\omega_\pm^2}{c^2} + k_\pm^2\right)\overleftrightarrow{I} - \vec{k}_\pm\vec{k}_\pm\right]\vec{E}_\pm = -\frac{4\pi i}{c^2}\,\omega_\pm\,\vec{j}_\pm \quad (*) \qquad \text{(I-7)}$$

In order to arrive at a dispersion relation, we have to express $j_\pm$ in terms of the electric field $E_\pm$. This current $j_\pm$ arises due to the linear response of the electrons to the oscillating field $E_\pm$ and the beat of the incident wave $E_{o\pm}$ (**) with density fluctuations δn at k, ω. Thus we get

$$\vec{j}_\pm = \sigma_\pm\,\vec{E}_\pm + q\,\delta n\,(\vec{k},\,\omega)\,\vec{v}_{o\pm} \qquad \text{(I-8)}$$

where $\vec{v}_{o\pm} = -\frac{e}{im_e\omega_o}\,\vec{E}_{o\pm}$. The conductivity σ can be described in terms of the dielectric constant ε through

$$\sigma_\pm = i\omega_\pm\,\frac{1}{4\pi}\,(\varepsilon_\pm - 1) \quad (***) \qquad \text{(I-9)}$$

Inserting the expression in (I-7) we find

$$\left[\left(k_\pm^2 - \frac{\omega_\pm^2}{c^2}\,\varepsilon_\pm\right)\overleftrightarrow{I} - \vec{k}_\pm\vec{k}_\pm\right]\vec{E}_\pm = -\frac{\omega_p^2}{c^2}\,\frac{\delta n_e}{n_o}\,(\vec{k},\,\omega)\,\vec{E}_{o\pm}(\pm\omega_o) \qquad \text{(I-10)}$$

The first term in (I-8) modifies the vacuum part of equation (I-7) into one for a medium by setting $\varepsilon_\pm \neq 1$. The second term of eq. (I-8) as it appears in equation (I-10) describes directly the generation of fields at $\vec{E}_\pm(\omega_\pm)$ due to the beat of the incident field $\vec{E}_{o\pm}(\pm\omega_o)$ with the density fluctuations $\delta n(\omega)$.

* $\overleftrightarrow{I} = \begin{pmatrix} 1 & 0 & 0 \\ 0 & 1 & 0 \\ 0 & 0 & 1 \end{pmatrix}$

** $\vec{E}_{o\pm} = \vec{E}_o(+\omega_o) + \vec{E}_o(-\omega_o)$

*** This is a general relationship for electromagnetic waves in conducting media and follows from Maxwell's equations.

It will later be of mathematical convenience to solve for $E_\pm$ by inverting (I-10). The result is

$$\vec{E}_\pm = -\omega_p^2 \frac{\delta n_e}{n_o} \left[\left(\overleftrightarrow{I} - \frac{\vec{k}_\pm \vec{k}_\pm}{k_\pm^2} \right) \frac{1}{D_\pm} - \frac{\vec{k}_\pm \vec{k}_\pm}{k_\pm^2 \omega_\pm^2 \varepsilon_\pm} \right] \vec{E}_{o\pm} \tag{I-11}$$

There, $D_\pm = k_\pm^2 c^2 - \omega_\pm^2 \varepsilon_\pm$ (I-12)

with $\vec{k}_\pm = \vec{k} \pm \vec{k}_o$, $\omega_\pm = \omega \pm \omega_o$,

$\varepsilon_\pm = 1 - \frac{\omega_p^2}{\hat{\omega}_\pm^2}$ and $k_o^2 c^2 - \omega_o^2 + \omega_p^2 = 0$

This form will be used later.

After the equation for the electromagnetic fields (I-11) has been established, we now proceed to calculate the density fluctuations $\delta n_e(k, \omega)$ arising from the beat of the incident and the scattered lightwave $\vec{E}_{o\pm}(\pm\omega_o)$ and $\vec{E}_\pm(\omega_\pm)$ by solving the Vlasov equation. To do this, the ponderomotive force concept first has to be introduced.

We wish to solve, at least approximately, the equation of motion for a single electron in an electromagnetic field which is a slow function of position in the sense that its strength varies only slightly within the range of amplitude of the electron due to the oscillation in this field.

In zero order approximation, the electron will oscillate in the applied field according to

$$\vec{\xi} = \frac{e}{m_e \omega^2} \vec{E} \quad \text{where } \vec{E} = \vec{E}_o (e^{i\omega t} + e^{-i\omega t}) \tag{I-14}$$

All other symbols have the usual obvious meaning. The electron will, however, additionally experience a slow movement due to the fact that the electric field $\vec{E}$ is not constant along the coordinates of oscillation.

We therefore expand

$$\vec{E} = \vec{E}(\vec{R}) + (\delta\vec{R}\,\nabla)\,\vec{E} \qquad \text{(I-15)}$$

Choosing $\delta R = \xi$ means to ask: how much does $\vec{E}$ change if the electron position is changed during the oscillation. An effect of equal order arises because the electron not only oscillates in a pure electric field but in the electromagnetic field of the light wave.

The complete equation of motion can approximately be written as

$$m(\ddot{\vec{R}} + \ddot{\vec{\xi}}) = -e\left[\vec{E}(\vec{R}) + (\vec{\xi}\cdot\nabla)\,\vec{E} + \dot{\vec{\xi}} \times \vec{B}\right] \qquad \text{(I-16)}$$

with $\dot{\vec{\xi}} = -\frac{e}{i\omega m}\vec{E}$, $\vec{\xi} = \frac{e}{m\omega^2}\vec{E}$ (I-17)

and $\frac{\partial\vec{B}}{\partial t} = -\nabla \times \vec{E}$ hence $\vec{B} = -\frac{1}{i\omega}\nabla \times \vec{E}$ (I-18)

We see that the second and third terms of the R.H.S. of equation (I-16) result in motion at the frequencies 0 and 2ω, respectively. As high frequencies (2ω) are of no interest here, we can finally write the low-frequency part of the equation (I-16) as

$$m\ddot{\vec{R}} = -\frac{e^2}{2m\omega^2}\left[(\vec{E}\cdot\nabla)\vec{E} + \vec{E} \times (\nabla \times \vec{E})\right] \qquad \text{(I-19)}$$

The first term arises from the spatial non-uniformity of the electric field and is a drift term analogous to the $(v\nabla)v$ term in fluid equations; the second term is due to the influence of the magnetic part of the electromagnetic field on the electron and is a force pointing along the vector of propagation of the electromagnetic wave.

Rewriting

$$\vec{E} \times (\nabla \times \vec{E}) = \nabla\vec{E}^2 - (\vec{E}\nabla)\vec{E} \qquad \text{(I-4)}$$

we see that both forces combine to form a <u>ponderomotive force</u> $m\ddot{R}$ which can be derived from a ponderomotive potential ψ given by

$$m\ddot{\vec{R}} = -\nabla\psi = -\frac{e^2}{2m\omega^2}\nabla\vec{E}^2 \qquad \text{(I-20)}$$

It must be understood that this force varies slowly with time, e.g. $\ddot{\xi} >> \ddot{R}$ and thus at frequences at which ions can respond via self-consistent fields. If the described calculation is carried out for more than one electromagnetic wave the ponderomotive potential is found to be[14]

$$\psi = \frac{e^2}{2m}\,\mathrm{Re}\,\left|\sum_{\lambda}\frac{\vec{E}_{\lambda}}{i\omega_{\lambda}}\right|^2 \qquad \text{(I-21)}$$

In the case considered here, there are three fields present, $\vec{E}_o(\pm\omega_o)$, $\vec{E}_+(\omega_+)$ and $\vec{E}_-(\omega_-)$.

An explicit evaluation of (I-21) for these three fields shows that the ponderomotive potential for the slow frequency of the plasma wave at ω is given by

$$\psi_{\omega} = \frac{e^2}{2m\omega_o^{\,2}}\left(\vec{E}_{o+}\,\vec{E}_- + \vec{E}_{o-}\,\vec{E}_+\right) \qquad \text{(I-22)}$$

We now turn to the problem of calculating the induced density fluctuations with the Vlasov equation. It should be understood that an electron in a plasma experiencing a strong electromagnetic field is subject to three forces at two types of frequencies:

The direct force of the electric part of the incident electromagnetic field $\vec{E}_o(\omega_o)$ which makes the electron oscillate at ω_o, a force due to the self-consistent field between ions and electrons arising from local density perturbations, and a force derived from the ponderomotive potential. The ions, on the other hand, are considered only to experience a force due to the self-consistent fields, since the direct

effect on them via the incident electromagnetic field and the ponderomotive force is smaller than that for electrons by a factor of $\sim \frac{q_i/m_i}{q_e/m_e}$ *.

To calculate a distribution function f_i for ions and f_e for electrons we therefore write**

$$\frac{\partial f_i}{\partial t} + \vec{v}_i \nabla f_i + \frac{1}{m} (Z e \nabla \phi) \frac{\partial f_i}{\partial v_i} = 0 \qquad \text{(I-23)}$$

$$\frac{\partial f_e}{\partial t} + v_e \nabla f_e - \frac{1}{m} [e \nabla (\Phi + \frac{\Psi}{e})] \frac{\partial f_e}{\partial v_e} = 0 \qquad \text{(I-24)}$$

As the ponderomotive potential appears only as a modification of the self-consistent potential both equations can be solved by an expansion $f = f_o + f^1$ around the equilibrium distribution function f_o as is shown in any textbook on plasma physics[16-19] and the result for the density fluctuations is

$$\delta n_e = \frac{k^2}{4\pi e} (\Phi + \frac{\Psi}{e}) \chi_e \qquad \text{(I-25)}$$

$$\delta n_i = \frac{k^2}{4\pi e} \Phi \chi_i \; ^{\dagger} \qquad \text{(I-26)}$$

The third equation for the three unknowns δn_e, δn_i and Φ is Poisson's equation.

$$- k^2 \Phi = 4\pi (e \, \delta n_i - e \, \delta n_e) \qquad \text{(I-27)}$$

Eliminating δn_i out of (I-26) and (I-27) and then eliminating Φ out of the remaining two equations yields

---

* charge-to-mass ratio for electrons/ions.

** ϕ is the self-consistent potential in the plasma

† χ_e, χ_i see p. 14

$$\delta n_e = -(1 \pm \chi_i)\, \chi_e \frac{k^2}{4\pi e^2} \frac{\Psi}{\varepsilon} \tag{I-28}$$

Ψ is the ponderomotive potential due to the beat of the incident and the scattered electromagnetic wave and is given by (I-22).

With equation (I-28) the second goal is achieved, namely the description of how density fluctuations are set up due to the beat of two electromagnetic waves in a plasma.

It remains to extract a dispersion relation out of the two equations (I-28) and (I-11).

Equations (I-11) and (I-28) are a set of coupled equations for $\vec{E}_\pm$ and δn. Combining (I-28) and (I-22) and replacing in the resulting expression E_+ and E_- from (I-11) one can cancel out δn_e. The resulting equation is the wanted dispersion relation

$$1 = \frac{(1+\chi_i)\chi_e}{\varepsilon} \frac{k^2}{4\pi m \omega_o^2} \frac{\omega_p^2}{n_o} \left[\vec{E}_{o+} \left(\left[(\overleftrightarrow{I} - \frac{\vec{k}\,\vec{k}}{k^2}) \frac{1}{D_+} - \frac{\vec{k}\,\vec{k}}{k^2\omega^2\varepsilon} \right] \vec{E}_{o+} \right) + \right.$$
$$\left. + \vec{E}_{o-} \left(\left[(\overleftrightarrow{I} - \frac{\vec{k}\,\vec{k}}{k^2}) \frac{1}{D_-} - \frac{\vec{k}\,\vec{k}}{k^2\omega^2\varepsilon} \right] \vec{E}_{o-} \right) \right] \tag{I-29}$$

In order to bring this expression into the more familiar form appearing in Ref. 14 note that

$$\frac{\varepsilon}{(1+\chi_i)\chi_e} = \frac{1}{\chi_e} + \frac{1}{1+\chi_i} \quad \text{and}$$

$$\vec{E}_o [(\vec{k}\cdot\vec{k})\, \vec{E}_o] = |\vec{E}_o \cdot \vec{k}|^2 = E_o^2 k^2 \sin^2(\measuredangle\, \vec{E}_o, \vec{k})$$

so that

$$\vec{E}_o \left[(\overleftrightarrow{I} - \frac{\vec{k}\cdot\vec{k}}{k^2})\, \vec{E}_o \right] = \vec{E}_o^{\,2} k^2 [1 - \sin^2(\measuredangle\, \vec{E}_o, \vec{k})] = |\vec{k} \times \vec{E}_o|^2$$

Substituting $\omega_p^2 = \frac{4\pi n_o e^2}{m}$ and remembering that $-\frac{e}{im\omega_o}\vec{E}_o$ was the 0 order quiver velocity of the electron in the incident field $\vec{E}_o$ one arrives at the final form of the dispersion relation

$$\frac{1}{\chi_e} + \frac{1}{1+\chi_i} = k^2\left[\frac{|\vec{k}_+ x \vec{v}_o|^2}{D_+ k_+^2} + \frac{|\vec{k}_- x \vec{v}_o|^2}{D_- k_-^2} - \frac{|\vec{k}_+ \cdot \vec{v}_o|^2}{k_+^2\omega_+^2\varepsilon_+} - \frac{|\vec{k}_- \cdot \vec{v}_o|^2}{k_-^2\omega_-^2\varepsilon_-}\right] \qquad \text{(I-30)}$$

From the derivation of (I-30) it follows that the $\vec{k}\cdot\vec{v}_o$ terms in the R.H.S. of (I-30) arise from the grad div $\vec{E}$ term in the initial wave equation (I-5), e.g. from the electrostatic components at the sideband frequencies ω_+ and ω_-. The $\vec{k}$ x $\vec{v}_o$ terms arise from the $-\Delta + \frac{1}{c}\frac{\partial^2}{\partial t^2}$ term in the wave equation (I-5), e.g. from the electromagnetic components at the sideband frequencies. The reason for both of these modes depending on each other is that the term $-\frac{4\pi i}{c^2}\omega_\pm j_\pm$ (eq. I-7) involves a coupling via the ponderomotive force of the electrostatic components.

To get a feeling for how this dispersion relation describes the propagation of a density wave and electromagnetic sideband modes as a function of each other, consider the following simplified case: imagine some kind of process where only the second term in (I-30) on the R.H.S. is of importance, e.g. $D_- \to 0$, and where the ions can be neglected. Then, (I-30) reduces to

$$\left(\frac{1}{\chi_e} + 1\right) D_- = \frac{k^2}{k_-^2}\,|\vec{k}_- x v_o|^2 \qquad \text{(I-31)}$$

If there would be no ponderomotive force term, then the R.H.S. of equation (I-31) would be zero and the equation would reduce to

$$\left(\frac{1}{\chi_e} + 1\right)\cdot D_- = 0 \qquad \text{(I-32)}$$

Then one solution is $\frac{1}{\chi_e} + 1 = 0$ and, hence, $\omega^2 = \omega_p^{\ 2}$ describes an undisturbed plasma oscillation at ω_p; or $D_- = 0$ hence, $k_-^{\ 2}c^2 + \omega_p^{\ 2} = \omega_-^{\ 2}$ describes the undisturbed propagation of an electromagnetic wave at frequency ω_- through that plasma.

The R.H.S. of (I-31) therefore, arising due to the ponderomotive force, is the coupling coefficient between the electromagnetic wave at ω_- and the plasma oscillation at ω_p. The strength of this coupling is clearly proportional to k^2, i.e. the length of the wave vector of the density fluctuation squared. This means that short wavelength fluctuations will couple stronger to the electromagnetic sideband modes than long wavelength fluctuations, and the coupling is proportional to the intensity of the incident electromagnetic wave at ω_o.

The susceptibilities χ_i and χ_e are given through the Vlasov equation in terms of the equilibrium distribution function f_o by[14-19]

$$\chi_{e,i} = \frac{\omega_{pe,i}^2}{k^2} \int d^3v \, \frac{\vec{k} \frac{\partial f_{oe,i}}{\partial v}}{\omega - \vec{k}\cdot\vec{v}} \tag{I-33}$$

For f_o being Maxwellian, χ_e and χ_i have the following approximate forms which will be used throughout the calculations:

$$\begin{aligned}
&\text{for } \frac{\omega}{k} \gg v_e && \chi_e = -\frac{\omega_{pe}^{\ 2}}{\omega^2} \\
&\frac{\omega}{k} \ll v_e && \chi_e = \frac{1}{k^2\lambda_{De}^2}(1 + I_e) \\
&\frac{\omega}{k} \gg v_i && \chi_i = -\frac{\omega_{pi}^{\ 2}}{\omega^2} \\
&\frac{\omega}{k} \ll v_i && \chi_i = \frac{1}{k^2\lambda_{Di}^2}(1 + I_i)
\end{aligned} \tag{I-34}$$

Here, with $v_i \ll v_e$, $I_{i,e}$ are the imaginary parts of the susceptibilities. Note that waves with large k (short wavelength) are strongly damped, waves with small k (long wavelengths) are weakly damped.

1.4 Specialization for stimulated backscattering

Consider the case where an incident electromagnetic wave decays into a plasma wave and a scattered electromagnetic wave. For the case of a reasonably underdense plasma ($\omega_o^2 >> \omega_p^2$) the electromagnetic wave will propagate according to $D \approx 0$, therefore the $\vec{k} \times \vec{v}_o$ terms in (I-30) will dominate. At moderate incident powers $E_o{}^2$, predominantly downconversion (generation of electromagnetic sideband modes at $\omega - \omega_o$ rather than $\omega + \omega_o$) will occur, so that the D_+ term can be neglected since it is non resonant.

This reduces (I-30) to

$$\frac{1}{\chi_e} + \frac{1}{1+\chi_i} = \frac{k^2|\vec{k}_- \times \vec{v}_o|^2}{k_-{}^2 D_-} \qquad \text{(I-35)}$$

The R.H.S. of this equation shall now be simplified using physical arguments.

For underdense plasmas, the dispersion relation for the light and plasma waves show that $\omega << \omega_o$ and ω_-, hence $|\vec{k}_o| \approx |\vec{k}_-|$. $|\vec{k}|$ however need by no means be small and because the coupling coefficient in (I-35) is proportional to k^2, the instability will occur at large rather than at small k.

These considerations lead to the following possibilities to arrange $\vec{k}_o$, $\vec{k}_-$ and $\vec{k}$:

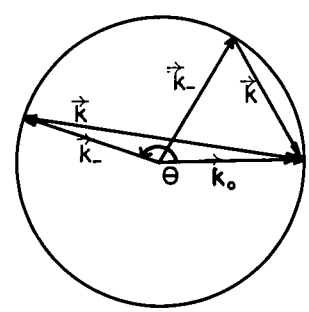

For all cases the diagram shows that $|\vec{k}\ | \approx 2|\vec{k}_o|\cos\theta$ which is as approximate as $|\vec{k}_-| \approx |\vec{k}_o|$ and means that the instability will predominantly occur at $\vec{k}_- \approx -\vec{k}_o$, that is the electromagnetic sideband mode at ω_- will be backscattered and $\vec{k}$ will be about $2\vec{k}_o$. This means that the density fluctuation will propagate parallel to the incident light wave vector.

Therefore, $\dfrac{|\vec{k}_- \times \vec{v}_o|^2}{k_-^{\,2}}$ can be written as

$$\frac{|\vec{k}_- \times \vec{v}_o|^2}{k_-^{\,2}} \approx v_o^{\,2} \sin^2\phi$$

with ϕ the angle between $\vec{k}$ and $\vec{v}_o$ being near 90°.

We now try to simplify D_-, also using physical arguments. Introducing damping for the light wave means that

$$D_- = k_-^{\,2}c^2 - \omega_-^{\,2} + \omega_p^{\,2} \text{ is complex because } \omega_o = \omega_- + \omega$$

where ω_o is now written as $\omega_o + i\,\Gamma_o$.

Using $k_o^{\,2}c^2 - \omega_o^{\,2} + \omega_p^{\,2} = 0$, the expression for D_- reduces to

$$D_- = 2\omega_o\left(\omega + \frac{k^2c^2}{2\omega_o} - \frac{\vec{k}\cdot\vec{k}_o c^2}{\omega_o} + i\,\Gamma_o\right)$$

Including all these approximations in (I-35), one obtains

$$\frac{1}{\chi_e} + \frac{1}{1+\chi_i} = \frac{k^2 v_o^{\,2}\sin^2\phi}{2\omega_o\left(\omega + \dfrac{k^2c^2}{2\omega_o} - \dfrac{\vec{k}\cdot\vec{k}_o c^2}{\omega_o} + i\Gamma_o\right)} \qquad \text{(I-36)}$$

Using the dispersion relations for the incident and the scattered light wave together with the approximations

$$(\omega_o^{\,2} - \omega_-^{\,2}) \approx 2\omega_o(\omega_o - \omega_-) \quad \text{and}$$

$$(k_o^{\,2} - k_-^{\,2}) \approx -2\,k\,k_o + k^2$$

It follows that

$$-\frac{\vec{k}\cdot\vec{k}_o c^2}{\omega_o} - \frac{k^2c^2}{2\omega_o} \approx \omega_o - \omega_- = \Delta\omega \qquad \text{(I-37)}$$

$\Delta\omega$ is the difference between the incident and the scattered light wave which has to be equal to the frequency of the plasma wave.

The dispersion relation therefore takes the following form:

$$\frac{1}{\chi_e} + \frac{1}{1+\chi_i} = \frac{k^2 v_o^{\,2} \sin^2\phi}{2\omega_o(\omega - \Delta\omega + i\Gamma_o)} \qquad \text{(I-38)}$$

It should be remembered that, according to the approximations made, this dispersion relation describes the decay of an incident electromagnetic wave into a plasma wave (ion or electron) and a <u>back</u>scattered electromagnetic wave in a plasma that is underdense enough so that $D_- \approx 0$.

Three distinct cases of instabilities exist:

(1) The scattering plasma wave is largely undamped and hence close to an eigenmode. If the scattering occurs off electron waves, the process is called "Stimulated Raman Scattering"; if it occurs off ion waves, it is called "Stimulated Brillouin Scattering" henceforth abbreviated SBS.

(2) If either mode is strongly damped, the processes are called "scattering off resistive quasi modes".

(3) Finally, there is a more exotic form of this type of instability which occurs at too high powers to concern us any further.[14] This is termed "scattering off reactive quasi modes". It refers to the case where the frequency shift $\omega_o - \omega_-$ is larger than the eigenfrequency of the plasma oscillation.

As the Landau damping of the plasma wave depends critically on the parameter $k\lambda_D$, with λ_D being the Debye shielding distance, the distinction between the first two cases will be formulated mathematically by $k\lambda_D \lesssim 1$ or $k\lambda_D \gg 1$ respectively.

1.5 Stimulated Brillouin Scattering

As stimulated scattering off ion modes was observed in the experiment described later, this case shall now be treated in some detail. First, consider the case where the ion wave is only weakly damped. Then, the susceptibilities can be written as (see I-34)

$$\chi_e \approx \frac{1}{k^2\lambda_D^2} \quad , \quad \chi_i \approx -\frac{\omega_{pi}^2}{\omega_i^2}$$

hence,
$$\frac{1}{\chi_e} + \frac{1}{1+\chi_i} = \frac{k^2\lambda_D^2(\omega^2 - \omega_{pi}^2) + \omega^2}{\omega^2 - \omega_{pi}^2}$$

$$= \frac{(1 + k^2\lambda_D^2)\left[\omega^2 - \frac{\omega_{pi}^2 k^2\lambda_D^2}{1+k^2\lambda_D^2}\right]}{\omega^2 - \omega_{pi}^2}$$

with $\omega_i^2 = \omega_{pi}^2 \frac{k^2\lambda_D^2}{1+k^2\lambda_D^2}$ and including weak Landau damping, e.g. $\omega_i^2 \rightarrow \omega_i^2 - 2i\Gamma_a\omega_i$ (I-38) can be written as:

$$(\omega^2 - \omega_i^2 + 2i\,\Gamma_a\omega_i)(\omega - \Delta\omega + i\Gamma_o) = \frac{k^2 v_o^2 \sin^2\phi(\omega^2 - \omega_{pi}^2)}{2\omega_o(1+k^2\lambda_D^2)} \qquad \text{(I-39)}$$

Thereby $\Delta\omega$ is, according to its definition, about equal to ω_i. In order to find regions of instability, one sets $\omega = \omega_i + i\gamma$, multiplies out the L.H.S., and separates real and imaginary parts. The real part describes the actual dispersion of the waves and the imaginary part, if negative, the damping; if positive, the growth of the ion wave as a function of time.

Setting $\gamma = 0$ means to ask for the conditions under which the wave neither grows nor decays with time which describes the threshold for the

instability. The result for the growthrate γ is

$$\gamma = -\frac{1}{2}\left[\Gamma_o + \Gamma_a - \sqrt{(\Gamma_o - \Gamma_a)^2 + \frac{k^2 v_o^{\,2}(\sin^2\phi)\omega_{pi}^{\,2}}{\omega_o\omega_i(1+k^2\lambda_D^{\,2})}}\right] \qquad \text{(I-40)}$$

Note that the damping rates Γ_o, Γ_a are passive plasma parameters. The driving term that determines when threshold is obtained and how large the growthrate at threshold will be is

$$\frac{k^2 v_o^{\,2}\omega_{pi}^{\,2}\sin^2\phi}{\omega_o\omega_i(1+k^2\lambda_D^{\,2})}$$

When this term increases (e.g. with increasing input power) the value of the root increases until it is larger than the sum of the two damping rates, at which point the instability grows.

The threshold condition for weak damping ($k^2\lambda_D^{\,2} << 1$) and backscattering ($\phi = 90^o$) is calculated from (I-40):

$$4\Gamma_o\Gamma_a = \frac{k^2 v_o^{\,2}\omega_{pi}^{\,2}}{\omega_o\omega_i}\sin^2\phi \qquad \text{(I-41)}$$

Note that the threshold decreases as the plasma density decreases and the temperature increases and that it goes to zero with the damping of either the light wave or the ion acoustic wave going to zero.*

To find the growthrate just above threshold for $\Gamma_a >> \Gamma_o$ we expand the root into a Taylor series around Γ_a to get

$$\gamma_{\text{at threshold}} = \frac{k^2 v_o^{\,2}\omega_{pi}^{\,2}\sin^2\phi}{4\omega_o\omega_i(1+k^2\lambda_D^{\,2})\Gamma_a} \qquad \text{(I-42)}$$

---

*see also page 29

Large growthrates are obtained when the driving term becomes dominant as compared to the damping terms.

Then the growthrate is

$$\gamma_{max} = \frac{1}{2} \frac{k\, v_o\, \omega_{pi} \sin\phi}{\sqrt{\omega_o \omega_i (1 + k^2 \lambda_D{}^2)}} \qquad \frac{1}{2} \frac{k\, v_o\, \omega_{pi}}{\sqrt{\omega_o \omega_i}} \tag{I-43}$$

for $k^2\lambda_D{}^2 \ll 1$ and $\phi \quad 90^o$.

Next we consider the case where the ion wave is heavily damped ($k^2\lambda_D{}^2 \gtrsim 1$). This means for the susceptibilities (see I-34)

$$\chi_e = \frac{1}{k^2 \lambda_{De}{}^2} \quad ; \quad \chi_i = \frac{1 + I_i}{k^2 \lambda_{Di}{}^2}$$

for $T_e = T_i$ it is $\lambda_{Di}{}^2 = Z\, \lambda_{De}{}^2$, I_i is the imaginary part of χ_i

Inserting this into equation (I-38), setting $\omega = \omega_i + i\gamma$ but making no further assumptions on $k^2\lambda_D{}^2 \ll$ or $\gg 1$ we obtain

$$[\omega_i - \Delta\omega + i(\Gamma_o + \gamma)](Zk^2\lambda_D{}^2 + I_i + 1 + Z) = \frac{v_o{}^2 \sin^2\phi}{2\omega_o \lambda_D{}^2}(Zk^2\lambda_D{}^2 + I_i + 1) \tag{I-44}$$

solving the real part of this equation for ω_i and assuming I_i is small one obtains

$$\omega = \Delta\omega + \frac{v_o{}^2 \sin^2\phi}{2\omega_o \lambda_D{}^2} \cdot \frac{Zk^2\lambda_D{}^2 + 1}{Zk^2\lambda_D{}^2 + 1 + Z}$$

for strong Landau damping ($k^2\lambda_D{}^2 \gg 1$) this reduced to

$$\omega = \Delta\omega + \frac{v_o{}^2 \sin^2\phi}{2\omega_o \lambda_D{}^2} \tag{I-45}$$

To see what this expression means physically, we apply the arguments presented on p. 16,17 in reverse and find that the second term of eq. (I-45) can approximately be written as

$$\frac{v_o^{\,2}}{2\omega_o\lambda_D^{\,2}} \approx (\omega_o - \omega_-)\frac{v_o^{\,2}}{c^2}\frac{1}{k^2\lambda_D^{\,2}} \tag{I-46}$$

Hence, this term represents a frequency imprinted by the laser on the plasma that depends on the incident laser power and the amount of Landau damping.

Solving the imaginary part of (I-44) for the growthrate γ one obtains

$$\gamma = -\Gamma_o + \frac{v_o^{\,2}\sin^2\phi}{2\omega_o\lambda_D^{\,2}}\;\frac{I\,Z}{(Zk^2\lambda_D^{\,2} + 1 + Z)^2} \qquad \text{where } I = \frac{1}{i}\,I_i \tag{I-47}$$

This expression has various limits for $k^2\lambda_D^{\,2} \ll 1$, $\gg 1$ or ≈ 1

For strong Landau damping of the ion wave ($k^2\lambda_D^{\,2} \approx 1$) and $Z = 2$ the growthrate reduces to:

$$\gamma = -\Gamma_o + \frac{1}{25}\frac{v_o^{\,2}\sin^2\phi}{\omega_o\lambda_D^{\,2}}\;I \tag{I-48}$$

and the threshold becomes

$$\frac{v_o^{\,2}}{c^2} = \frac{25\Gamma_o\omega_o\lambda_D^{\,2}}{Ic^2} \tag{I-49}$$

one can see that this instability derives its existence from the magnitude of the imaginary part of the ionic susceptibility. This term being small means that the threshold is high, the growthrate small: Note that for $k^2\lambda_D^{\,2} \gg 1$ the result for threshold and growthrate depends much stronger on the magnitude of $k^2\lambda_D^{\,2}$.

1.6 The $\omega - k$ diagram

The section on stimulated Brillouin scattering shall be concluded by further interpreting stimulated backscattering on the so-called $\omega - k$ diagram. In the $\omega - k$ diagram ω and k are the axes of a Carthesian coordinate system and the curves represent the dispersion relations for light-, ion- and electron waves.

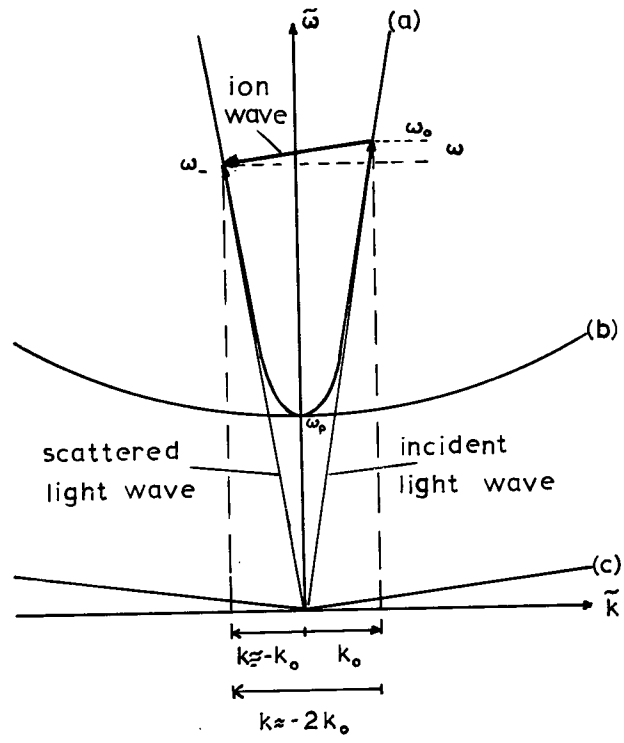

Figure (1-1): $\omega - k$ diagram. Curves are dispersion relations for (a) light, (b) electron, and (c) ion waves. Shown is the decay of a light wave into an ion acoustic wave and a scattered light wave.

Note that because $v_{ia} << v_e << c$, the dispersion curves for electron and ion waves are basically horizontal lines compared to the parabola representing the lightwave dispersion for small k.

Vectors ending on the light dispersion curve represent light waves and those ending on the electron wave dispersion curve represent electron waves, etc. Therefore, for a parametric decay process to be possible, its $\omega - k$ vectors have to add up.

Consider, as an example, the decay of a light wave into an ion acoustic wave and another light wave as shown in Fig. (1-1).

The projections on the frequency axis describe the conservation of energy: $\omega_o = \omega + \omega_-$. Because the frequency of the ion acoustic wave (ω) is small compared to the frequency of the light wave (ω_o), the frequency of the scattered light wave (ω_o) will be only slightly less than the frequency of the incident light wave. This is a general feature of Brillouin scattering. From the diagram, it also follows that the wave vector of the scattered light wave will be $-k_o$, with k_o being the wave vector of the incident light wave. Hence, k, the wave vector of the ion acoustic wave, will be $k \approx -2k_o$ (see p.16).

Furthermore the $\omega - k$ diagram shows that stimulated Brillouin scattering can only take place in underdense plasmas.

For the decay of e.g. a light wave into two electron waves[15], it is obvious that the process can only take place where $\omega_o \gtrsim 2\omega_p$ whereas the decay of a lightwave in an electron and an ion acoustic wave[15] can only occur at $\omega_o \gtrsim \omega_p$.

These are just some points which by no means exhaust the usefulness of the diagram. Questions about processes like cascading,*[15] parametric decay in moving plasmas etc., can also be answered by this simple picture.

*The Brillouin scattered light wave is intense enough to itself give rise to a higher order Brillouin scattered light wave.

1.7 Limitations of the theoretical model

The theoretical treatment of the described parametric instability shall be concluded by pointing out the limitations of the model used and its relevance to actual experiments.

Despite the use of Maxwell's and the Vlasov equations which are, for wave phenomena, quite general, the presented description is of very limited validity.

Firstly, only infinite, homogeneous plasmas were treated; secondly, a linearised theory only can describe the onset of instabilities; and thirdly, even in such simplified cases many approximations have to be made in order to arrive at analytically solvable equations. The linear theory for finite, inhomogeneous plasmas is considerably more complex and can be treated analytically only for very simple density profiles.[13,14] A presentation of that theory is considered well outside the scope considered here. However, a threshold expression for stimulated Brillouin scattering from this theory will be used later; its physical interpretation is given on p. 29. A complete theory describing the onset, growth and eventual saturation of parametric instabilities does not exist. At present, predictions that involve more complicated and detailed models are made with the aid of computer simulations.[2,4,30,47] Therefore, all that can be expected of the simple theory presented here, is to give an initial insight into the physics of parametric decay in plasmas and produce numerical values that provide order of magnitude estimates for thresholds and growthrates.

1.8 Numerical values for threshold and growthrate of stimulated Brillouin scattering in homogeneous and inhomogeneous plasmas

In order to evaluate the previous results numerically, the following list of formulas is handy:

Here, intensities are in $\frac{\text{watts}}{\text{cm}^2}$; temperatures in eV. As the cgs system is used, the dimensions of the results will be in cm, sec, esu, etc.*

(1) quiver velocity v_o $(\frac{\text{cm}}{\text{sec}})$ of an electron in an electric field of intensity I $(\frac{\text{watts}}{\text{cm}^2})$ for CO_2 laser wavelength

$$v_o = 265 \sqrt{I}$$

(2) Debye length λ_D (cm)

$$\lambda_D = 740 \sqrt{\frac{T}{n}} \quad ; \quad n \text{ in cm}^{-3} \quad , \quad T \text{ in eV}$$

(3) plasma frequency $(\frac{\text{rad}}{\text{sec}})$

$$\omega_{pe} = 5.6 \times 10^4 \sqrt{n} \quad ; \quad n \text{ in cm}^{-3}$$

(4) collision frequency between electrons v_{ee} $(\frac{1}{\text{sec}})$

$$v_{ee} = 2.8 \times 10^{-5} \frac{n}{T^{3/2}} \quad ; \quad n \text{ in cm}^{-3} \quad , \quad T \text{ in eV}$$

(5) collisional damping of a light wave in a plasma Γ_o $(\frac{1}{\text{sec}})$

$$\Gamma_o = 1.4 \times 10^{-24} \frac{n^2}{T^{3/2}} \quad ; \quad n \text{ in cm}^{-3} \quad , \quad T \text{ in eV}$$

(6) ion acoustic speed v_{ia} $(\frac{\text{cm}}{\text{sec}})$

$$v_{ia} = 6.9 \times 10^5 \sqrt{T_e} \quad ; \quad T \text{ in eV}$$

(7) electron thermal speed v_e $(\frac{\text{cm}}{\text{sec}})$

$$v_e = 6 \times 10^7 \sqrt{T_e} \quad ; \quad T \text{ in eV}$$

---

*incident laser light frequency is that of CO_2 laser light

(8) electrical conductivity σ(esu)

$$\sigma = 1.7 \times 10^{13} \frac{T^{3/2}}{Z} \qquad \text{(for He, Z = 2), T in eV}$$

The power of the CO_2 laser was $\sim$ 250 MW, focussed to about 1 mm^2. Hence the quiver velocity of an electron in this field is

$$v_o = 4.2 \times 10^7 \frac{cm}{sec} \quad *$$

or $$\frac{v_o^2}{c^2} = 1.9 \times 10^{-6}$$

Using the formulae p. 26, the thresholds and growthrates reduce to the following expressions (valid only for $\frac{\omega_p^2}{\omega_o^2} << 1$)

A) Stimulated scattering off quasi resistive ion modes

Growthrate $$\gamma = -1.4 \times 10^{-24} \frac{n^2}{T^{3/2}} + 1.8 \times 10^{-6} \frac{n}{T} \frac{1}{\sqrt{1 + 2 \times 10^{13} \frac{T}{n}}}$$

Threshold $$\frac{v_o^2}{c^2} = 1.6 \times 10^{-24} \frac{n}{\sqrt{T}} \sqrt{1 + 2 \times 10^{13} \frac{T}{n}}$$

B) Stimulated scattering off ion modes

Growthrate $$\gamma_{max} = 1.65 \times 10^{-2} (T_e n)^{\frac{1}{2}}$$

Threshold for a homogeneous plasma

$$\frac{v_o^2}{c^2} = 4.3 \times 10^{-39} \frac{n^2}{T^{5/2}}$$

Threshold for an inhomogeneous plasma[15] **

$$\frac{v_o^2}{c^2} = 6.8 \times 10^9 \frac{T}{n L_T}$$

where L_T is the scale length of temperature gradient in cm.

---

* Note that this is about the electron thermal speed in a plasma of some eV.

** In this expression, the Landau damping rate was neglected compared to the collisional damping rate.

Numerical values

A) scattering off quasi resistive modes

γ \ n	10^{15}	10^{16}	10^{17}	10^{18}
T_e = 1 eV	1.8×10^{9}	1.8×10^{10}	1.7×10^{11}	4×10^{11}
T_e = 10 eV	1.6×10^{8}	1.8×10^{9}	1.7×10^{10}	1.4×10^{11}
T_e = 100 eV	1×10^{7}	1.6×10^{8}	1.8×10^{9}	1.7×10^{10}

$\frac{v_o^2}{c^2}$ \ n	10^{15}	10^{16}	10^{17}	10^{18}
T_e = 1 eV	1.6×10^{-9}	1.6×10^{-8}	1.0×10^{-7}	1.6×10^{-6}
T_e = 10 eV	5.5×10^{-10}	5×10^{-9}	5×10^{-8}	5×10^{-7}
T_e = 100 eV	2.8×10^{-10}	1.8×10^{-9}	1.6×10^{-8}	1.6×10^{-7}

B) scattering off ion modes

γ \ n	10^{15}	10^{16}	10^{17}	10^{18}
T_e = 1 eV	5.2×10^{5}	1.6×10^{6}	5.2×10^{6}	1.6×10^{7}
T_e = 10 eV	1.6×10^{6}	5.2×10^{6}	1.6×10^{7}	5.2×10^{7}
T_e = 100 eV	5.2×10^{6}	1.6×10^{7}	5.2×10^{7}	1.6×10^{8}

thresholds for a homogeneous plasma

$\frac{v_o^2}{c^2}$ \ n	10^{15}	10^{16}	10^{17}	10^{18}
T_e = 1 eV	4.3×10^{-9}	4.3×10^{-7}	4.3×10^{-5}	4.3×10^{-3}
T_e = 10 eV	1.4×10^{-11}	1.4×10^{-9}	1.4×10^{-7}	1.4×10^{-5}
T_e = 100 eV	4.3×10^{-14}	4.3×10^{-12}	4.3×10^{-10}	4.3×10^{-8}

B) thresholds for an inhomogeneous plasma $L_T = 1$ mm*

$\frac{v_o^2}{c^2}$ \ n	10^{15}	10^{16}	10^{17}	10^{18}
T = 1 eV	6.9×10^{-6}	6.9×10^{-7}	6.9×10^{-8}	6.9×10^{-9}
T = 10 eV	6.9×10^{-5}	6.9×10^{-6}	6.9×10^{-7}	6.9×10^{-8}
T = 100 eV	6.9×10^{-4}	6.9×10^{-5}	6.9×10^{-6}	6.9×10^{-7}

*It may be surprising to see that the threshold for a homogeneous plasma increases with increasing density, however, the threshold for an inhomogeneous plasma decreases with increasing density.
The reason is that in deriving the threshold expression for a homogeneous plasma the assumed model was that density fluctuations have to be induced against the randomizing effect of damping (see p. 4). Hence, the threshold $\frac{v_o^2}{o^2} \sim \Gamma_o \Gamma_a$, is proportional to the product of the damping rates for ion and light wave. In deriving the threshold expression for an inhomogeneous plasma[12,14,15] however, the assumed model is that the induced density waves travel out of the region where the wave vector matching condition for stimulated scattering is satisfied and that compared to this instability suppressing effect, damping is negligible. Hence the threshold derived for that case depends on $\frac{1}{L_T}$, the inverse temperature scale length of the plasma.

CHAPTER 2

Experimental investigation of the backscattered and transmitted CO_2 laser light

2.1 Introduction

The purpose of the CO_2 laser light scattering experiments was to investigate which instabilities could be detected with the CO_2 laser power available and the plasma parameters given by the Z-pinch.

As the theory shows, stimulated scattering should manifest itself in large amounts of backscattered light.

We therefore measured the amount of backscattered CO_2 laser light under different plasma conditions (e.g. as a function of the collapse phase of the pinch).

As the spectral decomposition of the backscattered CO_2 laser light will show which stimulated backscattering process takes place, we searched the backscattered light for signals at the following frequencies (ω_o being the frequency of the incident CO_2 laser light):

near ω_o, to detect stimulated Brillouin scattering and possibly cascading[15]

near $\frac{3}{2}\omega_o$, to detect two plasmon decay[14,15,20,23]

near $\frac{1}{2}\omega_o$, to detect stimulated Raman scattering at $\frac{1}{4}$ the critical density[14,15,22]

The transmitted or forward scattered light was searched near ω_o to look for

- the normal transmission of CO_2 laser light through an underdense plasma
- filamentation*[14,15,24,25]
- cascading*[15]

*see footnote p. 24

Additionally, the angular dependence of the CO_2 laser light backscattered due to stimulated Brillouin scattering was investigated as far as the setup allowed.

The results can be summarized as follows:

The only parametric instability that was detected with absolute certainty was stimulated Brillouin scattering. Due to the low threshold and high growthrate this instability is also of great importance for laser fusion experiments.[20]

Filamentation* was not present to a degree that it could have been detected. This is in agreement with simple theoretical models about this instability.[24,25] No other instability was found, most certainly because the CO_2 power available did not allow it to exceed any other thresholds.

The angular dependence of the backscattered CO_2 laser light shows a somewhat surprising result for which a plausible explanation will be presented.

---

*Filamentation is the ceration of low density channels by the laser light along its direction of propagation.

2.2 The Z-pinch plasma, measurements of radius, temperature and density and the CO_2 laser used for the laser-plasma interaction studies.

A detailed presentation of the design parameters and the discharge bank of the Z-pinch is given in Ref. 26. The description given here is only intended to provide the necessary background for the experiments described subsequently.

The Z-pinch consists of a pyrex glass vessel with hollow copper electrodes inserted in each end.*

5.6 kJ of electrical energy stored in a 84 μF capacitor bank are discharged into 1.2 Torr He to produce a pinch plasma which reaches maximum compression and temperature about 2 μsec after the initial breakdown.**

End on framing photography with a TRW image converter camera gave the first photographs of the collapsing plasma.[26] As this geometry did not allow a detailed observation of the phase of maximum compression, e.g. minimum radius, side on streak photography was used to spatially and temporally resolve this final phase of collapse.† These measurements revealed a minimum luminous radius of the plasma of 2 mm.

The first measurements of plasma temperature and density were done spectroscopically using the 4686Å line of He II.[26] For the means available at the time, these measurements yielded good estimates of a maximum density of $8 \times 10^{18} \frac{e}{cc}$ and a maximum temperature of 30 eV to 40 eV.

---

*For actual dimensions see specifications at end of report.

**see Fig. 5-2

† see footnote p. 33

Next, a Ruby laser Thomson scattering system* was set up to verify the measurements.[26] The attempt to use an Optical Multichannel Analyser** (OMA) to record the electron feature of the Thomson scattered spectrum resulted in the development of a technique that allowed the fast gating of the OMA without distortions. A description of this technique and its application to improved spectroscopical density measurements is presented in Chapter IV.

Before the signal-to-bremsstrahlung ratio in the Thomson scattered electron feature*** could be improved to yield a truly satisfactory spectrum however, the observation of the Thomson scattered ion feature permitted the making of very good measurements of plasma temperature and density.† These results are shown in Fig. (2-3) and will be used throughout this report.

The CO_2 laser used in the laser-plasma interaction studies was a Lumonix T600 module in unstable resonator configuration. In this laser, an electrical discharge transverse to the optical axis inverts the vibrational levels of CO_2 in a He.Ne.CO_2 mixture at atmospheric pressure. The large gain of the inverted medium allows the use of an unstable resonator for coupling out the laser light. The T600 module employed a confocal unstable resonator configuration as shown on the following page.

---

*see Ch. IV, Fig. 4-1.

**see specifications

***see Ch. IV.

†I am indebted to Brian Hilko for letting me use the results of his experimental work.

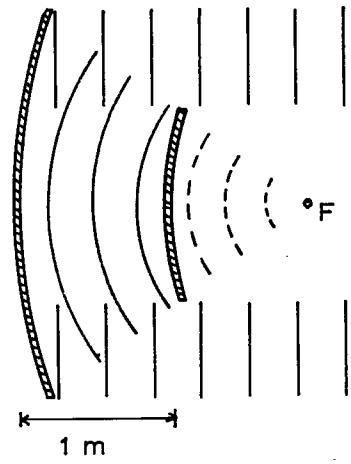

Figure (2-1): The unstable resonator of the Lumonix T600 TEA CO_2 laser.

Both mirrors have F as a common focal spot. Due to this arrangement, the wave leaving the cavity is a plane wave and the output aperture of the CO_2 laser has an annular shape as shown in Fig. (2-2) below.

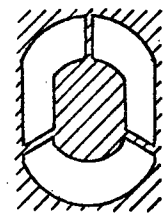

Figure (2-2): Annular output of the CO_2 laser due to the use of an unstable resonator cavity.

The height is 10.5 cm, the width 8 cm and equal to the separation of the electrodes between which the discharge pumping the laser transition takes place. This output aperture shape allowed the measurements which are described in 2.6 and evaluated in 3.23.

2.3 Experimental provisions

Before the CO_2 laser could successfully be focussed into the plasma, the pinch vessel had to be modified and new plasma parameters, now changed by these modifications, had to be measured.

The sketch below shows the principal setup to focus the CO_2 laser into the plasma.

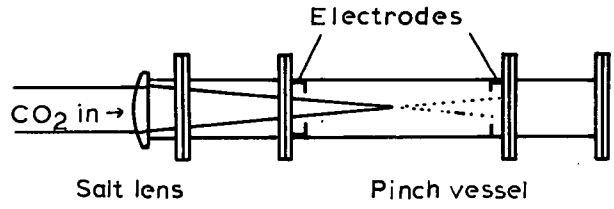

It is obvious that the laser light had to be protected from the plasma to actually be able to form a focal spot in the center of the vessel. Otherwise defocussing of the laser beam by the plasma would limit the power flux of the incident light to too low values.

The problem was solved by using a quartz funnel as indicated in the next sketch.

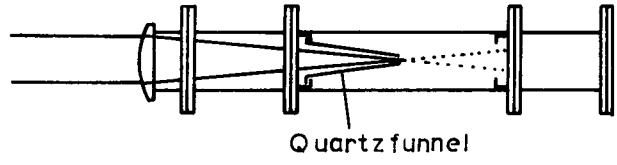

Quartz must be used as glass quickly suffers from a phenomenon called "crazing" which consists of myriads of very fine cracks, arising from the temperature shock due to absorbed UV radiation.* The funnel must be embedded in softer materials, e.g. nylon, otherwise the mechanical shock of the pinching plasma will destroy it within a very few shots.

*I am indebted to Ray Elton of N.R.L. for this information.

In order to measure the transmission of the CO_2 laser light, a second funnel has to be installed accordingly. It must be expected that these modifications change the plasma parameters. Therefore, the plasma density and temperature were measured also with both funnels installed. The time of maximum compression, e.g. minimum radius was measured with no, one and two funnels installed, using streak and shadow photography. These measurements were carried out within the program of Brian Hilko's Ph. D. work, hence, detailed comments and results will appear in his thesis.*

The results, as far as they are relevant for the experiments to be described, are shown in the Fig. (2-3) overleaf. The top trace in each picture shows the density; the bottom trace shows the temperature of the pinch plasma as a function of time. Time t = 0 is chosen as the time when $\frac{dI}{dt} = 0$**, I being the total current in the pinch as measured with a Rogowski coil.[26] The top and bottom picture (no and two funnels) are experimental data obtained through ion feature Thomson scattering. The error bars indicate the spread of individual data and the uncertainty with which temperature and density can be deduced from the experimental results. The middle picture (one funnel) is inferred from the other two. The shaded area indicates an estimated error. The time axes of all three pictures represent the true time lags from picture to picture. About the dashed line in the bottom picture, see section 3.1.

The additional data points in the density trace of the top picture are measurements from the Stark broadening of the 4686Å line of He I, described in 4.3.

---

*see footnote p. 33.

**This time reference will be used exclusively throughout the report.

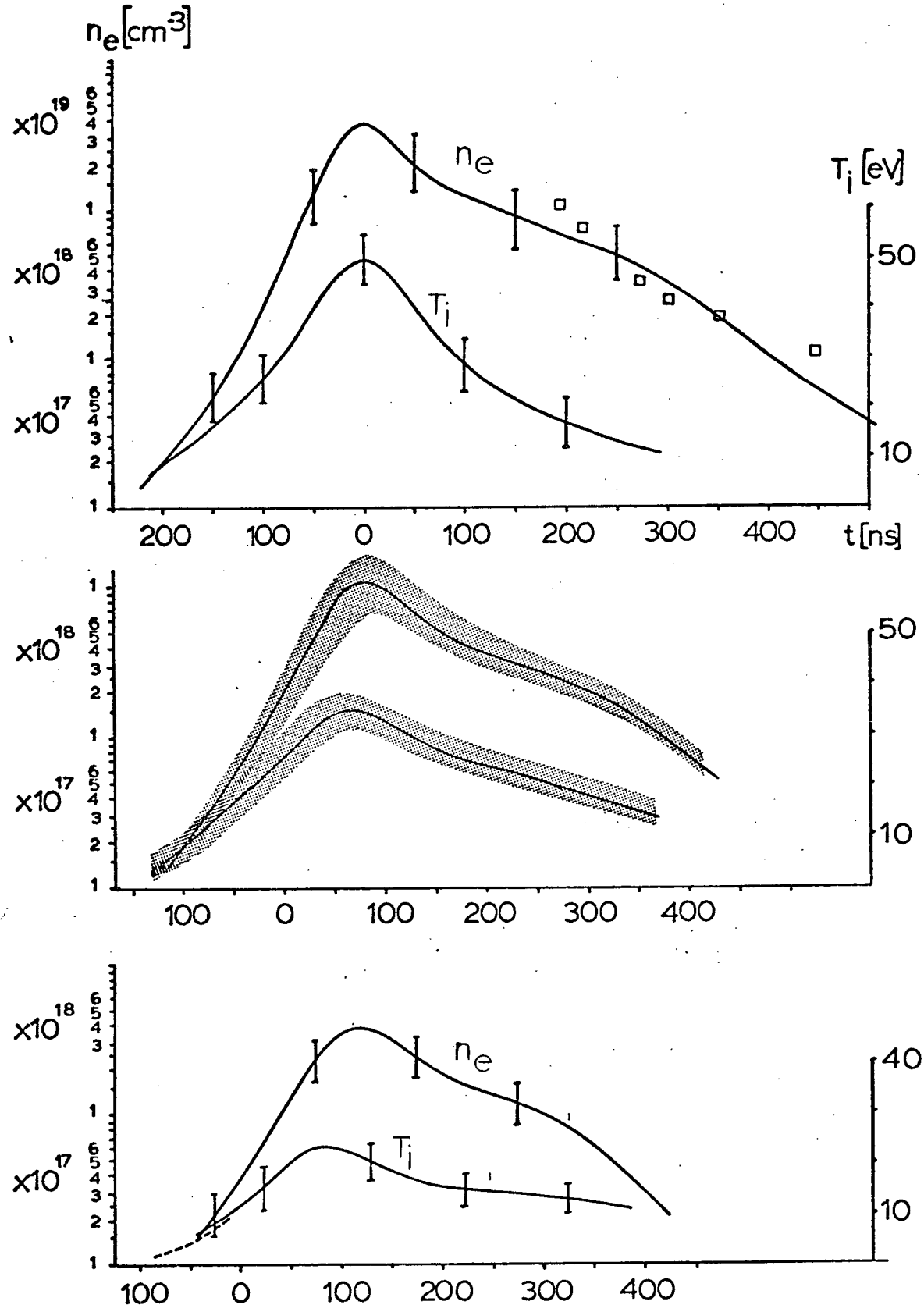
n_e [cm^{-3}]
x10^{19}
x10^{18}
x10^{17}
n_e
T_i
T_i [eV]
50
10
200
100
0
100
200
300
400
t [ns]
x10^{18}
x10^{17}
50
10
100
0
100
200
300
400
x10^{18}
x10^{17}
n_e
T_i
40
10
100
0
100
200
300
400

Figure (2-3)

The jitter of the pinch discharge was reduced from about 100 nsec to frequently less than 10 nsec by firing a preionization discharge in the vessel prior to the main pinch discharge. The actual circuit modification of the Z-pinch discharge bank is described in the appendix. This reduction in jitter naturally was of great importance in the spectral shot to shot scanning of the backscattered CO_2 laser light (see 2.5). An expensive problem (in terms of money) finally arises due to the fact that the plasma as it pinches is not confined axially. Part of it, therefore, is ejected with high speed through the hole in the cathode towards the salt lens (see e.g. Fig. 2.5). The resulting impact is sufficient to inflict visible mechanical damage particularly in the central region of the salt lens after 10 shots. The problem was solved partially by placing an obstacle in the plasma beam which is small enough to not hinder the incoming CO_2 laser light.

2.4 Spectrally integrated backscattered CO_2 laser light as a function of pinch-time.

The experimental setup is shown in Fig. (2-5) on the next page. Light scattered back from the plasma travels back out through the salt lens and onto the exit salt window of the CO_2 laser. This window is tilted and due to Fresnel reflection, ∿ 4% is reflected towards the Gen Tech* energy meter.

The result is shown in Fig. (2-4) below. The background, as later experiments showed, arises from the fact that the plasma itself radiates in the infrared.

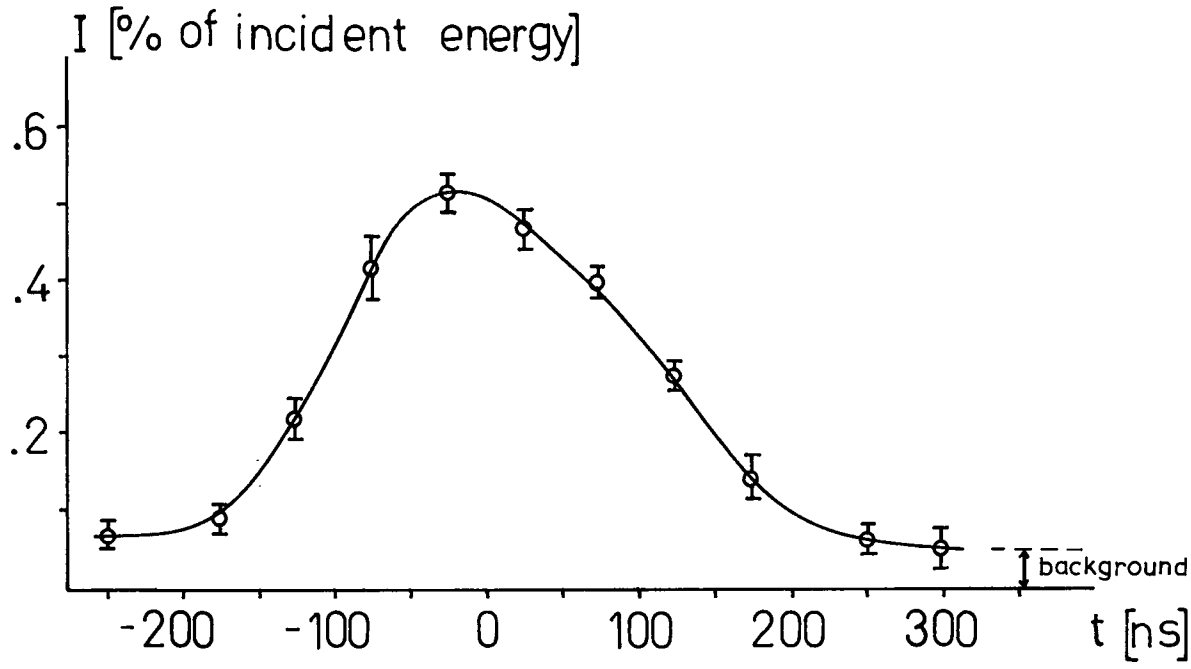

Figure (2-4): Spectrally integrated backscattered CO_2 laser light as a function of time. Error bars are standard errors of the mean.

---

*see specifications at end of report.

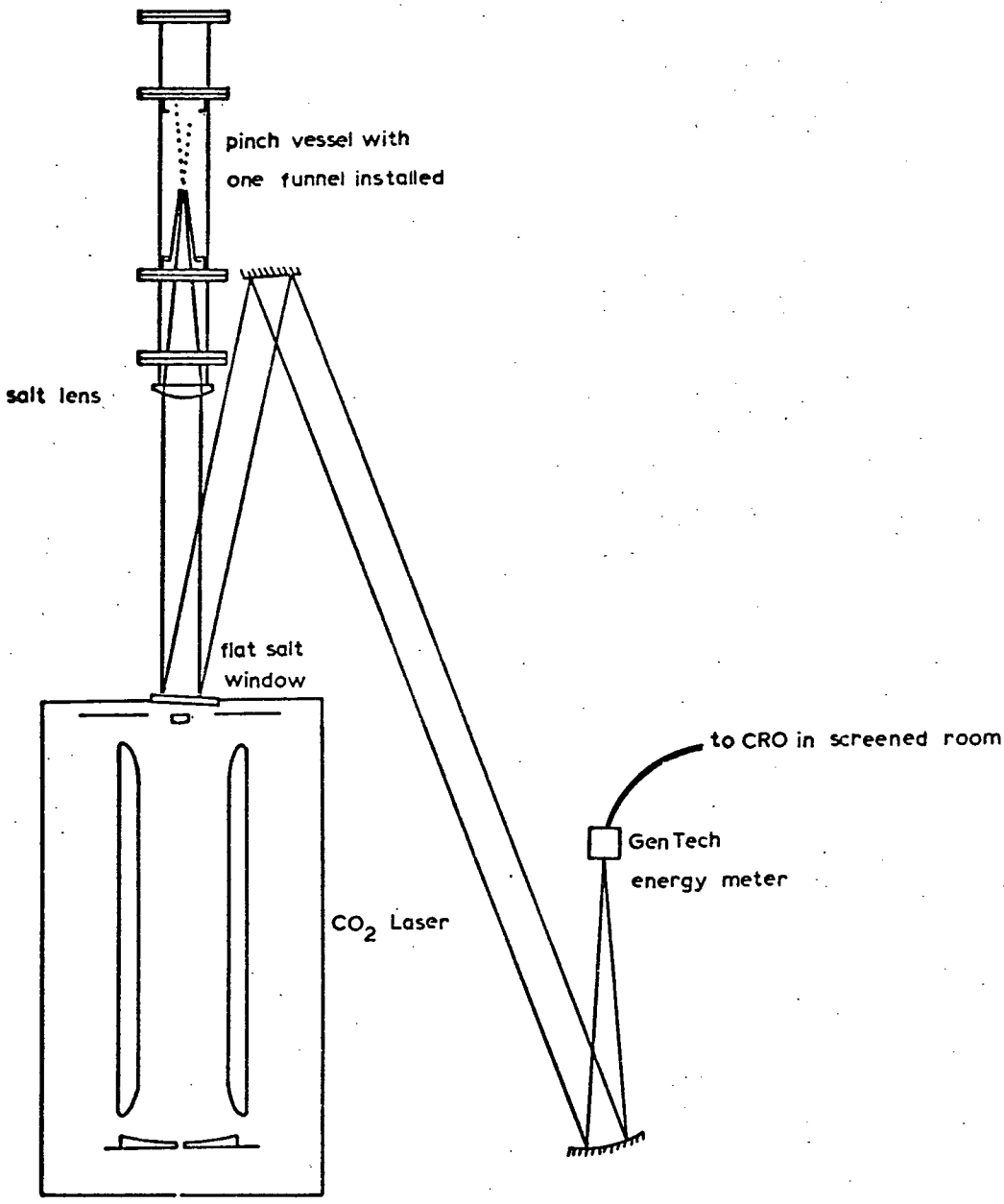

Figure (2-5): Setup for observing the spectrally integrated backscattered CO_2 laser light (section 2.4).

2.5 Spectrally integrated transmitted CO_2 laser light as a function of pinch-time.

The experimental setup is shown in Fig. (2-7) on the next page. For high transmitted energies, a calorimeter* was used as indicated. For lower transmitted energies a background again arises from the infrared emission of the plasma itself. These low energies were therefore measured with a gold doped germanium detector**, which time resolved the signal and thus allowed to discriminate against the infrared emission from the plasma. A typical oscilloscope trace is shown below.

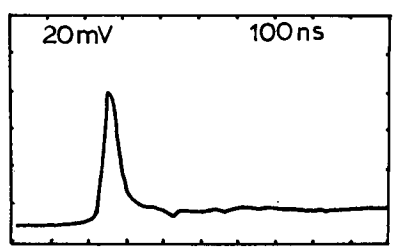

Figure (2-6): Transmitted CO_2 laser light with infrared emission from the pinch. Au Ge detector.

The results of the experiment are shown in Fig. (2-8) and Fig. (2-9).

---

*Apollo energy meter, see specifications at end of report

**see specifications

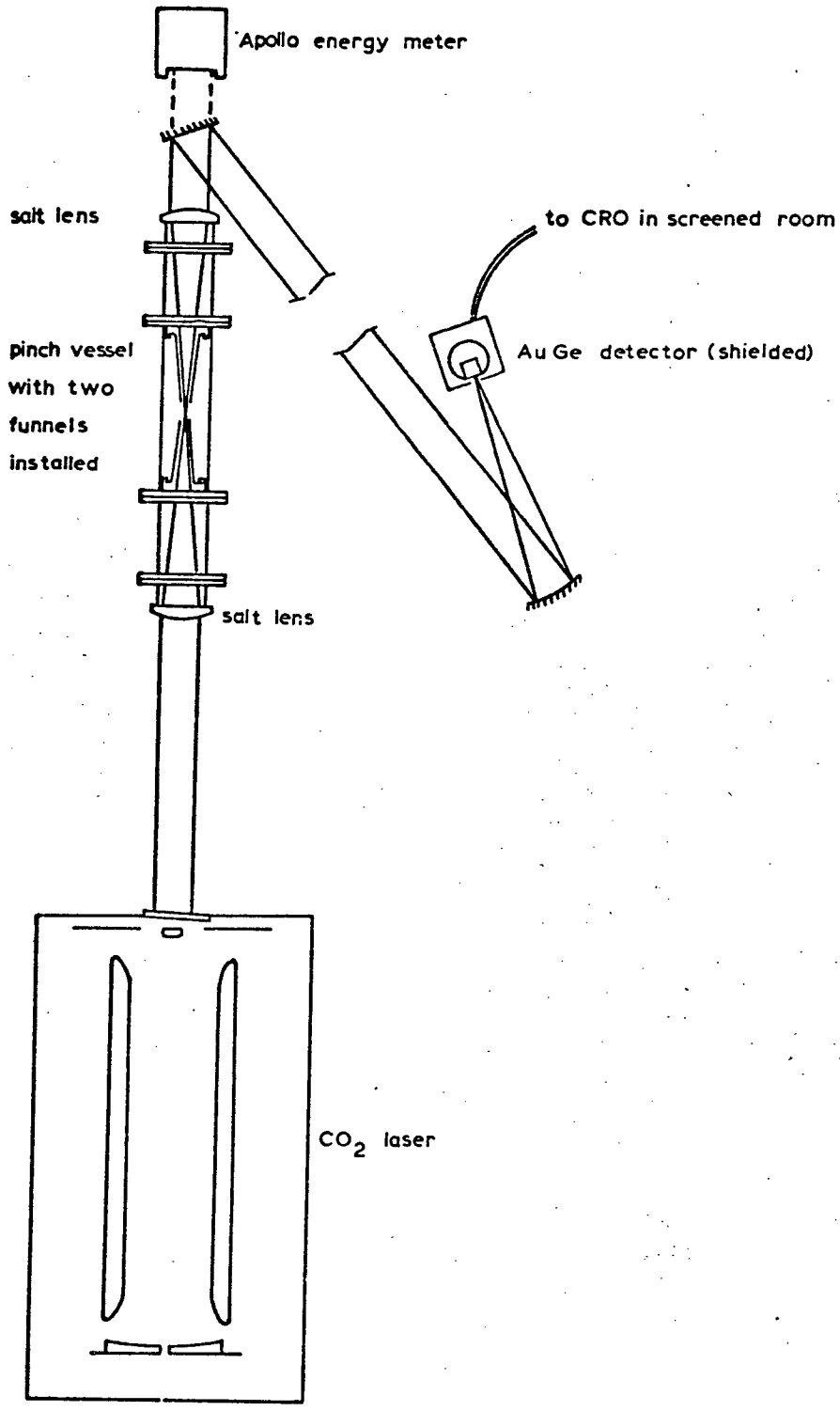

Figure (2-7): Setup to measure the transmitted CO_2 laser light (section 2.5).

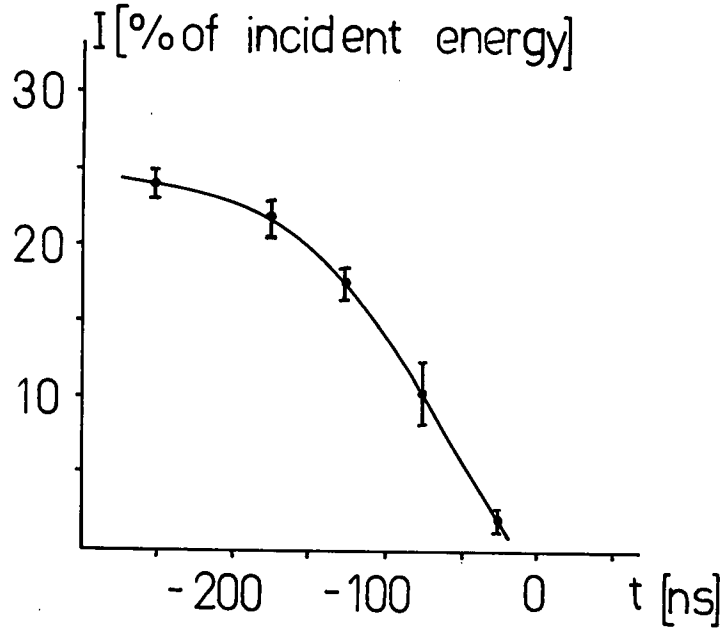

Figure (2-8): % of transmitted light as a function of time, Apollo energy meter. Error bars denote the standard error of the mean.

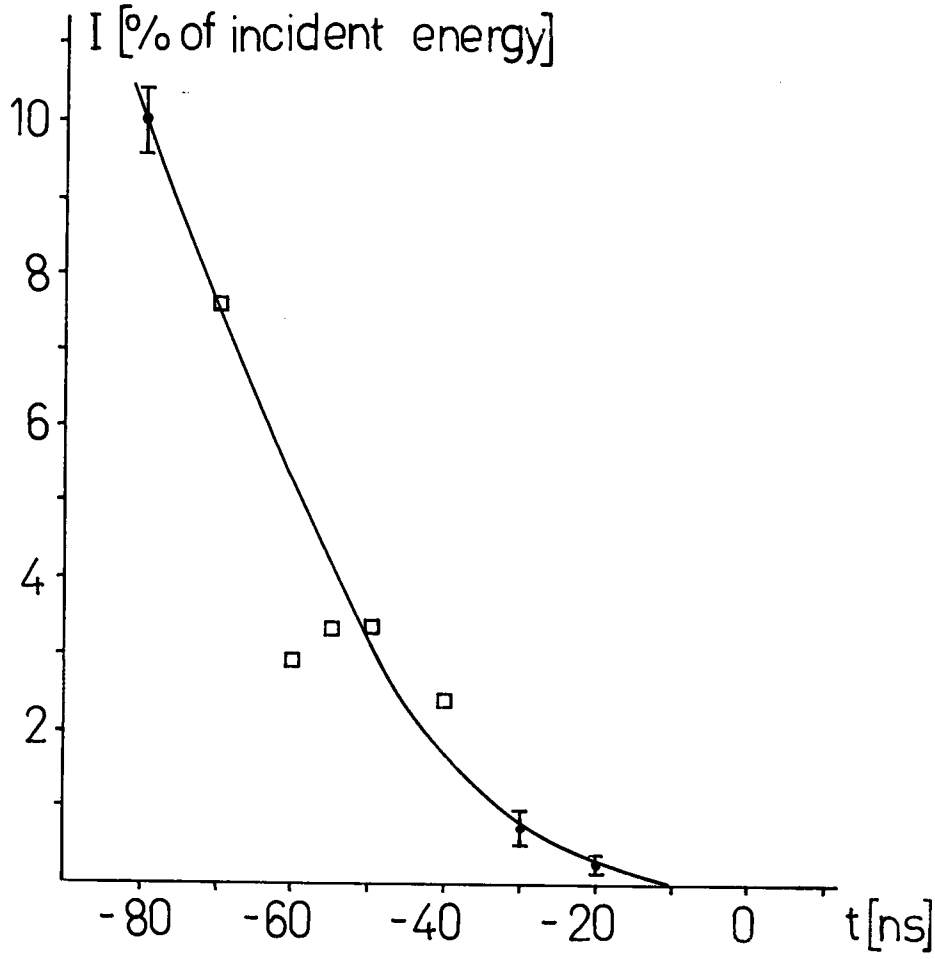

Figure (2-9): % of transmitted light as a function of time, Au Ge detector. Error bars denote the standard error of the mean; squares are single measurements.

2.6 Spectrally resolved backscattered CO_2 laser light at pinch time $t = 0 \pm 25$ nsec and the angular dependence of the backscattered light.

The experimental arrangement is shown in Fig. (2-10) on the next page. This setup was chosen for the following reasons:

Spherical mirrors, if used off axis, produce astigmatism. If they are additionally tilted out of the xy plane, this astigmatism appears rotated. The second plane mirror in Fig. (2-10) receiving the backscattered light serves to eliminate this rotation of astigmatism. The rest of the optics is set up to match the f number of the monochromator*, to keep the astigmatism at a minimum by imaging as little as possible off axis and, image as stigmatically as possible.

Finally, the choice of components was very limited.

Another problem arises due to the surface irregularities of the CO_2 laser output window. As it had to be used to reflect part of the backscattered light towards the detection optics, the sagittal focus at the entrance slit was not very sharp and much intensity was lost there.

To measure the angular dependence of the backscattered light, two types of masks were used on the mirror indicated in Fig. (2-10):

A Small Mask only reflected that light towards the detection optics that came back through the inner part of the CO_2 laser output annulus.**

A Big Mask only reflected light towards the detection optics that came directly back through the outer part of the annulus.

---

*see specifications at end of report

**see 2.2

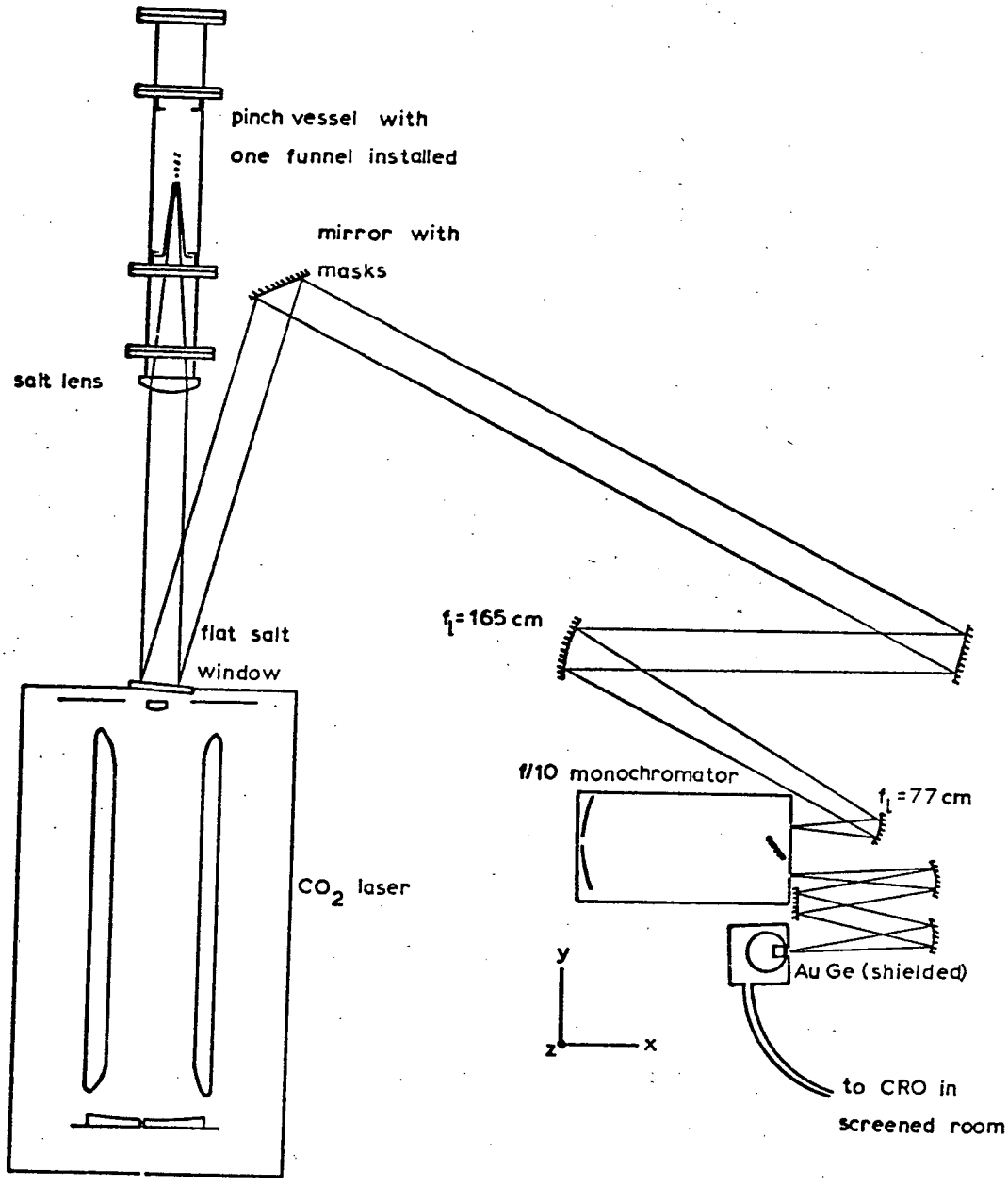

Figure (2-10): Setup to spectrally decompose the backscattered CO_2 laser light (section 2.6).

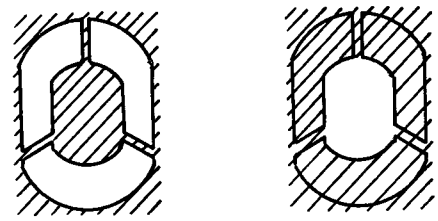

Big Mask Small Mask

Figure (2-11): Backscattered light was transmitted through the unshaded areas.

The spectral intensity distribution of light scattered back through the big mask and of light scattered back through the small mask is shown in Figs. (2-12) and (2-13).

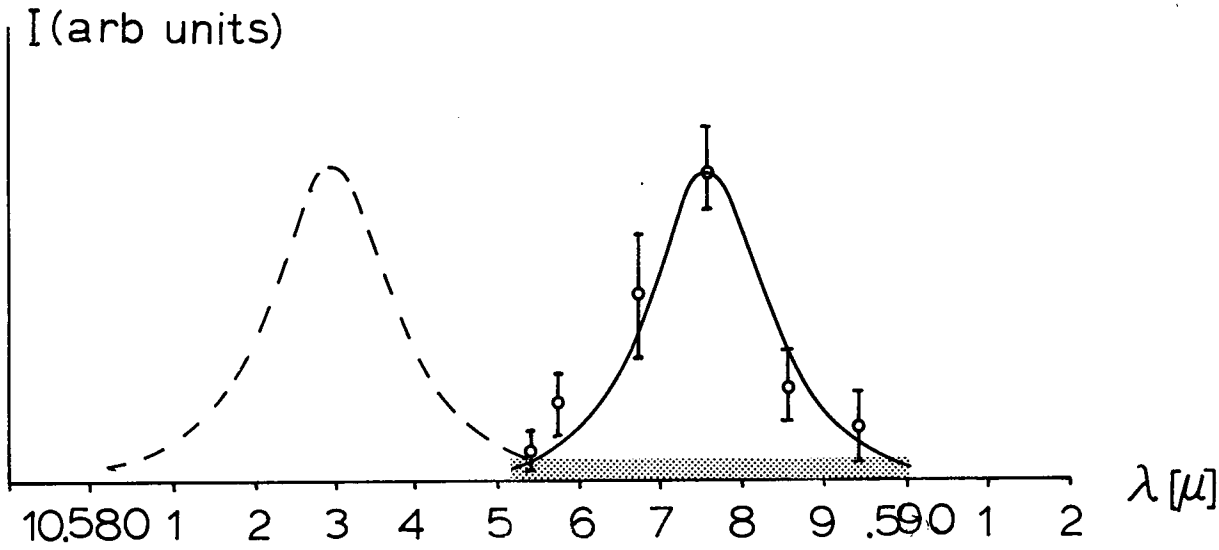

Figure (2-12): Spectral distribution of light scattered back through the big mask. The dashed line represents the unshifted CO_2 laser line. Its true width is small compared to the instrument profile. 100 μ slits. Error bars denote standard error of the mean; the shaded area shows the approximate noise level. Time is 0 ± 25 nsec.

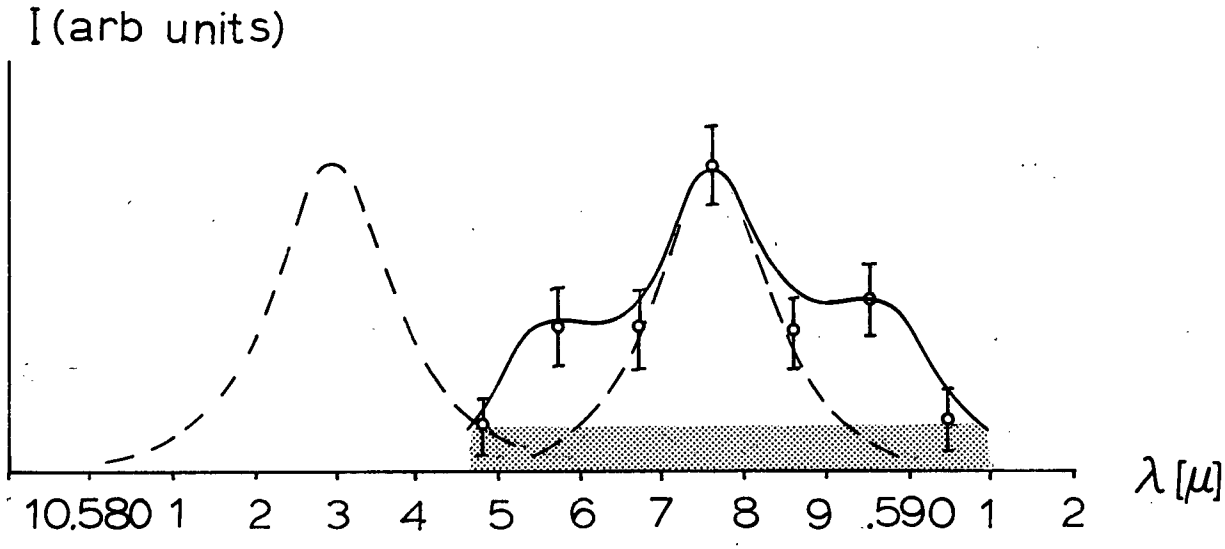

Figure (2-13): Spectral distribution of light scattered back through the small mask. The dashed line at 10.583 μ represents again the unshifted CO_2 laser line. Its true width is small compared to the instrument profile determined by 100 μ monochromator slits. Error bars denote standard error of the mean. The shaded area shows the approximate noise level. The vertical scale is 7.9 times that of Fig. (2-12). Time is 0 ± 25 nsec.

Fig. (2-13) shows that light scattered back through the inner part of the CO_2 laser output annulus is not only shifted in wavelength, but exhibits wings on both sides of the central line. A possible explanation for this effect is given in 3.24.

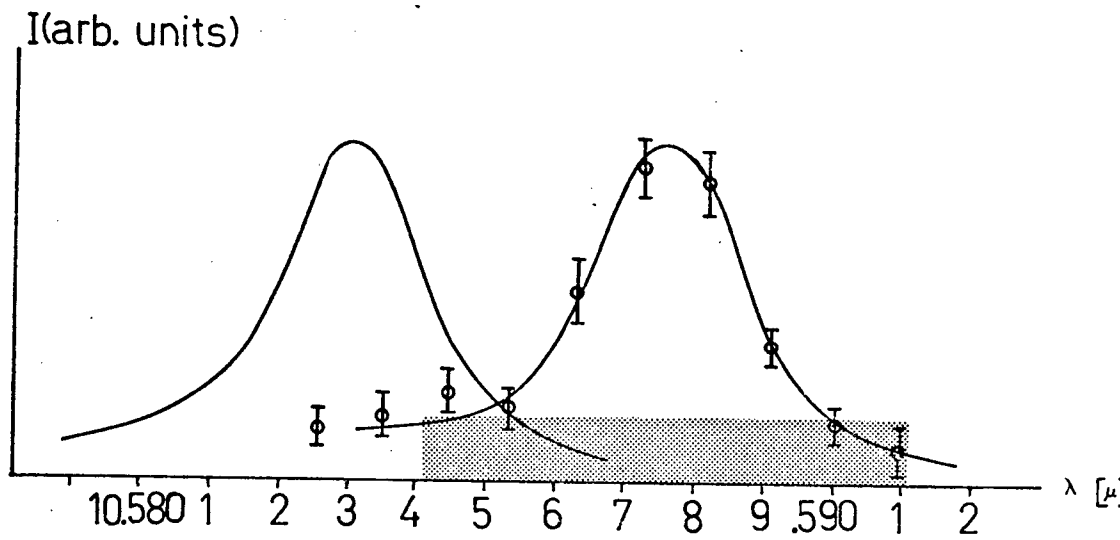

Figure (2-14): Spectrally resolved backscattered CO_2 laser light, no mask used. Left, the unshifted CO_2 laser line at 10.583 μ. Its width is the instrument width. Slits 130 μ, error bars denote standard error of the mean. Shaded area indicates the approximate noise level.
These data were taken at a much earlier date than those shown in Fig. (2-12) and (2-13).

CHAPTER 3

Evaluation of the experimental results

3.1 The transmitted CO_2 laser light

Fig. (3-1) shows the transmitted and backscattered intensity as a function of density as it can be condensed out of Fig. (2-3) and Figs. (2-4) and (2-9).

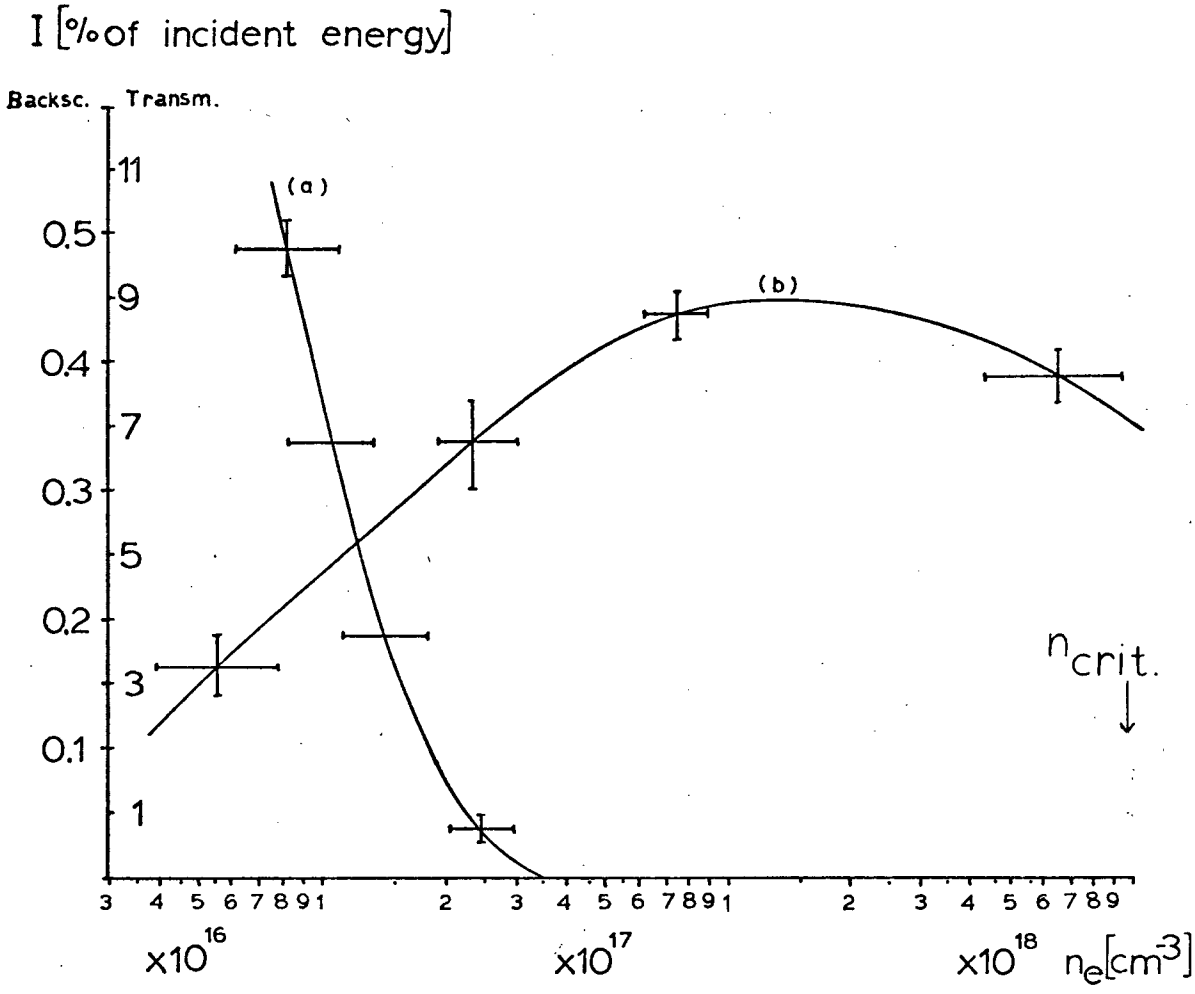

Figure (3-1): Backscattered (b) [one funnel installed] and transmitted (a) [two funnels installed] energy as a function of density of the plasma. Vertical error bars are experimental errors from Figs. (2-4) and (2-9), horizontal errorbars are due to density estimates from Fig. (2-3).

This measurement will now be compared with the theory of light absorption due to inverse bremsstrahlung (see also p.1).

The two funnels installed in the pinch vessel in order to be able to make these light transmission measurements (see Fig. (2-7)) left 2 cm of plasma between them. This, therefore, is the length over which the CO_2 laser light is absorbed. For the classical theory of inverse bremsstrahlung to be valid, the following requirements need to be satisfied.

(a) $\omega_o >> \omega_p$, e.g. the plasma must be quite underdense which is fulfilled.

(b) $\frac{e^2 E_o^2}{2m\omega_o^2} < k_B T$, e.g. the quiver energy of the electron in the field of the laser light must be small compared to the kinetic energy due to thermal motion which is fulfilled as well.

(c) $\frac{e^2 E_o^2}{2m\omega_o^2} < \hbar\, \omega_o^2$, i.e. the quiver energy of the electron in the field of the laser light must be so small that the energy of photons created by bremsstrahlung is not comparable to the photon energy absorbed in inverse bremsstrahlung. In our case, the two terms are comparable. Modifications in the classical expression for inverse bremsstrahling absorption however, only become necessary if $\frac{e^2 E_o^2}{2m\omega_o^2} >> \hbar\, \omega_o^2$, which is not the case for the experiment described.

In the Rayleigh Jeans limit for Planck's radiation law, the linear absorption coefficient can be written as

$$\kappa_B = n_e n_i \frac{64\pi^3 Z^2 e^6}{3\sqrt{6\pi}\, c\, \omega_o^2 (mkT)^{3/2}} G(T,\omega) \qquad \text{(III-1)}$$

For $\omega_o = \omega_{CO_2}$, $e^{\frac{\hbar\,\omega_{CO_2}}{k_B T}} \approx 1$, $Z\,n_e = n_i$ and $G(T, \omega_{CO_2}) \approx 2.5$,

this reduces to

$$\kappa_B = 7.06 \times 10^{-34} \frac{n_e^2}{T^{3/2}} \qquad \text{(III-2)}$$

Having ℓ cm of plasma, the intensity I of the transmitted light as a function of ℓ is given by

$$\frac{I(\ell)}{I_o} = e^{-\kappa_B \ell} \qquad \text{(III-3)}$$

In comparing the experiment with the theory however, the following problem arises:

As $\frac{I(\ell)}{I_o} = e^{-C \frac{n_e^2}{T^{3/2}} \ell}$, the relative error in the intensity ratio is

$$\frac{\Delta \frac{I(\ell)}{I_o}}{\frac{I(\ell)}{I_o}} \approx C \frac{n_e^2}{T^{3/2}} \ell \left[2 \frac{\Delta n}{n} + \frac{3}{2} \frac{\Delta T}{T} \right] \qquad \text{(III-4)}$$

where $\frac{\Delta n}{n}$ and $\frac{\Delta T}{T}$ are the relative errors in density and temperature so that for $\kappa\,\ell \gtrsim 1$, a 10% error in $\frac{\Delta n}{n}$ or $\frac{\Delta T}{T}$ leads to an order of magnitude error for the intensity ratio.

Taken however in the form

$$\kappa_B = -\frac{1}{\ell} \ln \frac{I(\ell)}{I_o} \qquad \text{(III-5)}$$

one can see from the reverse argument of (III-4) that a measurement of $\frac{I(\ell)}{I_o}$ allows a good determination of κ_B and hence of $n_e^2/T^{3/2}$, or one of the quantities if the other quantity is known.

According to the derivation of the above expression, T is the temperature of the plasma before the actual absorption process heats the plasma. The following table shows the values of κ_B computed from $\frac{I(\ell)}{I_o}$ and the values of T computed from κ_B and the densities given from Fig. (2-3).

Electron density $n_e[\frac{1}{cc}]$	$\frac{I(\ell)}{I_o}$ [%]	$\kappa[\frac{1}{cm}]$	T_e[eV]
8×10^{16}	10.3	1.14	2.5
9×10^{16}	8.9	1.21	2.8
1×10^{17}	7.6	1.29	3.1
1.5×10^{17}	3.3	1.71	4.4
2×10^{17}	1.5	2.10	5.7
2.5×10^{17}	.75	2.45	6.9
3×10^{17}	.30	2.90	7.8
3.5×10^{17}	∿.05	∿3.6	∿9

These calculated values for T_e are also shown as the dashed line in Fig. (2-3), bottom picture, where one can see that they connect well with the temperature curve measured by Thomson scattering.

It must be kept in mind that not all the CO_2 laser light that was not transmitted need actually be absorbed by inverse bremsstrahlung but can well be refracted out of the plasma.[28] This would lower the absorption coefficient κ_B and as a consequence increase the calculated electron temperature T.

Evidence for the complexity of the interaction volume is shown in the picture on the next page (Fig. 3-2).*

---

*Many thanks to Brian Hilko for letting me use this picture.

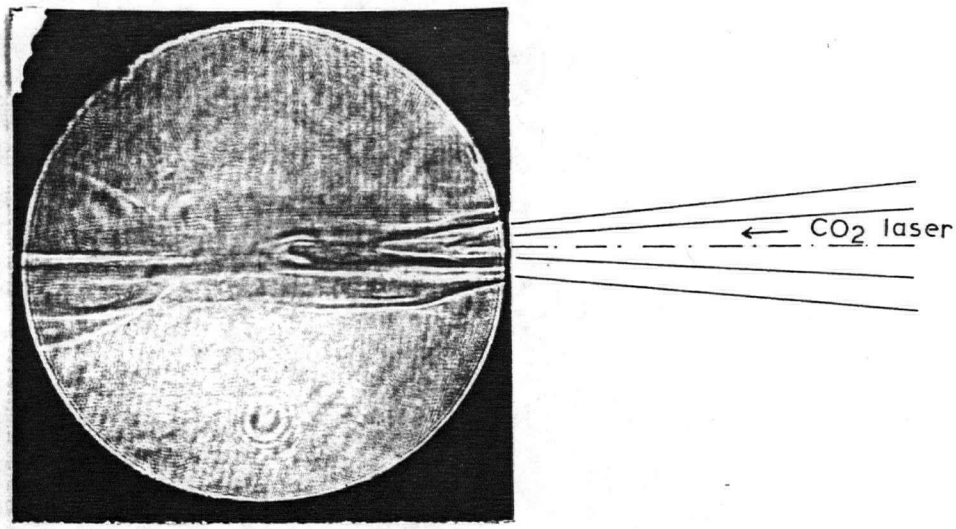

Figure (3-2): This photograph is a shadowgram done in Ruby laser light with the image plane ∿ 1 cm away from the plasma, viewed side on. The picture is magnified 3.4 times. The CO_2 laser is incident from the right. The vacuum focal spot is in the middle of the picture. The two funnels (see Fig. (2-7)) are just outside the picture to the left and right; time is - 30 nsec.*

It is evident that some plasma is pushed away by the CO_2 laser, that the beam is somewhat fanned out and bent away from its original direction and that it loses considerably in intensity as it penetrates the plasma.** The transmitted CO_2 laser light shows no shift off the CO_2 frequency of 10.583 μ.

The measured spectrum is shown in Fig. (3-3) on the following page. The result, to some extent, rules out modulational instabilities[11,12,14,15] resulting in sidebands in the foreward scattered light. At the given spectral

---

*The sharp light lines indicate the region where the incident CO_2 laser light has decreased the plasma density.

**The well-defined annular shape of the focal region is also indicated This fact will be of great importance for arguments presented in Section 3.24.

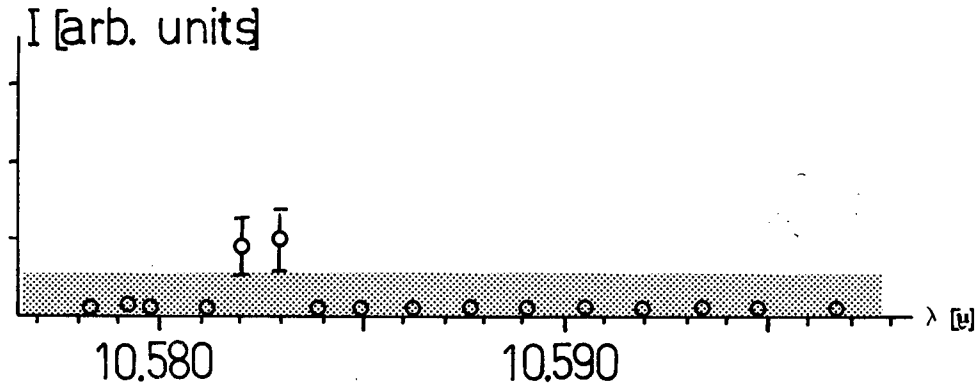

Figure (3-3): The spectrally resolved transmitted CO_2 laser light at pinch times < -20 nsec. Circles indicate the wavelength region scanned.* The shaded area denotes the noise level. The setup used was analogous to the ones shown in Fig. (2-7) and (2-10).

resolution the frequency shift resulting from such instabilities would have to be comparatively large to be observed. The occurrence of filamentation can principally not be ruled out; it is however, unlikely to occur as, for the relevant densities, homogeneous plasma thresholds are only just exceeded. This is in good agreement with estimates from other theories[24,25] which predict for our case a maximum density depression due to filamentation of $\frac{\Delta n}{n} \sim 5\%$.

Finally, there is, with the setup used, no possibility of distinguishing a minor filamental effect from simple light transmission through an underdense plasma (see, however, p. 76).

These arguments lead to the conclusion that the decrease in transmitted CO_2 laser light intensity is due to increasing inverse bremsstrahlung absorption of a plasma of increasing density.

---

*compare with Figs. (2-12) - (2-14).

3.2 The backscattered CO_2 laser light

The results of the experiments concerning the backscattered CO_2 laser light will be evaluated in the following sections:

3.21 Enhancement of the backscattered CO_2 laser light above thermal levels and the resulting ion wave amplitudes in the plasma.

3.22 Discussion of the observed wavelength shift of the backscattered CO_2 laser light.

3.23 Angular dependence of the backscattered CO_2 laser light and comparison with theory.

3.24 The wavelength dependence of the light backscattered through the 'small mask'.*

---

*see p. 46

3.21 Enhancement of the backscattered CO_2 laser light above thermal levels and the resulting ion wave amplitudes in the plasma.

In order to determine the enhancement of scattered light above thermal levels, the intensities scattered from thermal density fluctuations (Thomson scattering) must be known first.

The theory of Thomson scattering from plasmas* shows that the light intensity I_s as scattered from thermal fluctuation is given by

$$I_s(\alpha) = \frac{3}{8\pi} \sigma_T \, S(\alpha) \, I_{inc} \, N_e \frac{1}{r^2} (1 - \sin^2\theta \cos^2\phi) \qquad \text{(III-6)}$$

Here, $\sigma_T = .66 \times 10^{-24}$ cm^2 is the Thomson scattering crossection.

$$S(\alpha) = \frac{Z\alpha^4}{(1+\alpha^2)[1+\alpha^2(1+Z\frac{T_e}{T_i})]} \quad \text{for the ion feature}$$

$\alpha = \frac{1}{k\lambda_D}$, where k is the wave vector of the density fluctuation which does the scattering. λ_D is the Debye shielding distance.

I_{inc} = incident laser light intensity

N_e = number of electrons present within the scattering volume.

The last term on the R.H.S. of equation (III-6) describes the dipole field of the electron oscillating in the incident laser field in a coordinate system explained in Fig. (3-4) on the following page.

---

*41, 51

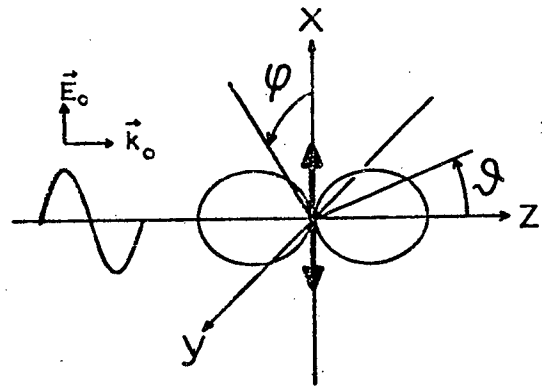

Figure (3-4): Explaining the coordinate system used in the calculations in Section 3.21. The dipole field is rotationally symmetric with respect to the x axis. The ϕ coordinate rotates around the Z axis. "Backscattering" means $\theta \rightarrow 180^o$.

In order to find the intensity scattered back through the pinch lens (see Fig. (2-5)), equation (III-6) will have to be integrated from $\phi = 0$ to 2π and $\theta = 180^o - \frac{\Delta\theta}{2}$ to 180°. There $\Delta\theta$ corresponds to the angle of the $\sim$ f/5 pinch lens, $\Delta\theta \approx \frac{1}{\text{f-number}}$ for f-numbers >> 1.

Assuming that the scattering occurs in the underdense region of the plasma, $|\vec{k}| \approx |2\vec{k}_o|$ (see p.16) so that $\alpha = \frac{1}{k\lambda_D} \approx \frac{1}{2k_o\lambda_D}$. For the densities and temperatures involved (see Fig. (2-3)) one can see that in all cases $\alpha >> 1$. With the plasma being a He-Plasma, $S(\alpha)$ then becomes $\approx \frac{2}{3}$. N_e, the number of electrons in the scattering volume is given by

$$N_e = n_e A_F \ell$$

where n_e is the electron density, A_F the focal area of the CO_2 laser, being $\sim 1\ mm^2$ and ℓ is the length of the interaction region.

Finally, we multiply eq. (III-6) by $\frac{1}{2}$ because only the long wavelength side of the Thomson scattered ion feature was observed as being enhanced.

Accounting for all these points, one arrives at

$$I_{BS}^{therm} = I_{inc} \times 8.13 \times 10^{-30}\, n_e \times \ell \qquad \text{(III-7)}$$

where now I_{BS} is in Joules, and I_{inc} is in Joules/cm^2.
With 27 Joules of incident CO_2 laser energy focussed to 1 mm^2 this reduces to

$$I_{BS}^{therm} = 2.2 \times 10^{-26}\, \ell \times n_e \qquad \text{(III-8)}$$

An "exact" value for ℓ is not known. Considering the geometry involved it is, however, reasonable to assume that it is of the order of a few mm. Supported by experimental evidence, (Fig. (3-2)), $\ell \sim 1$ cm was used. From formula (III-8) and Fig. (3-1), the enhancement $I_{BS}^{observed}/I_{BS}^{thermal}$ can be calculated. The results is plotted in Fig. (3-5) on the following page and shows that the intensity enhancement drops smoothly as the density of the plasma increases.

To truly understand the behaviour shown in Fig. (3-5) in terms of Stimulated Brillouin scattering it would be necessary to have detailed information about the temperature scale length of the plasma as a function of time.

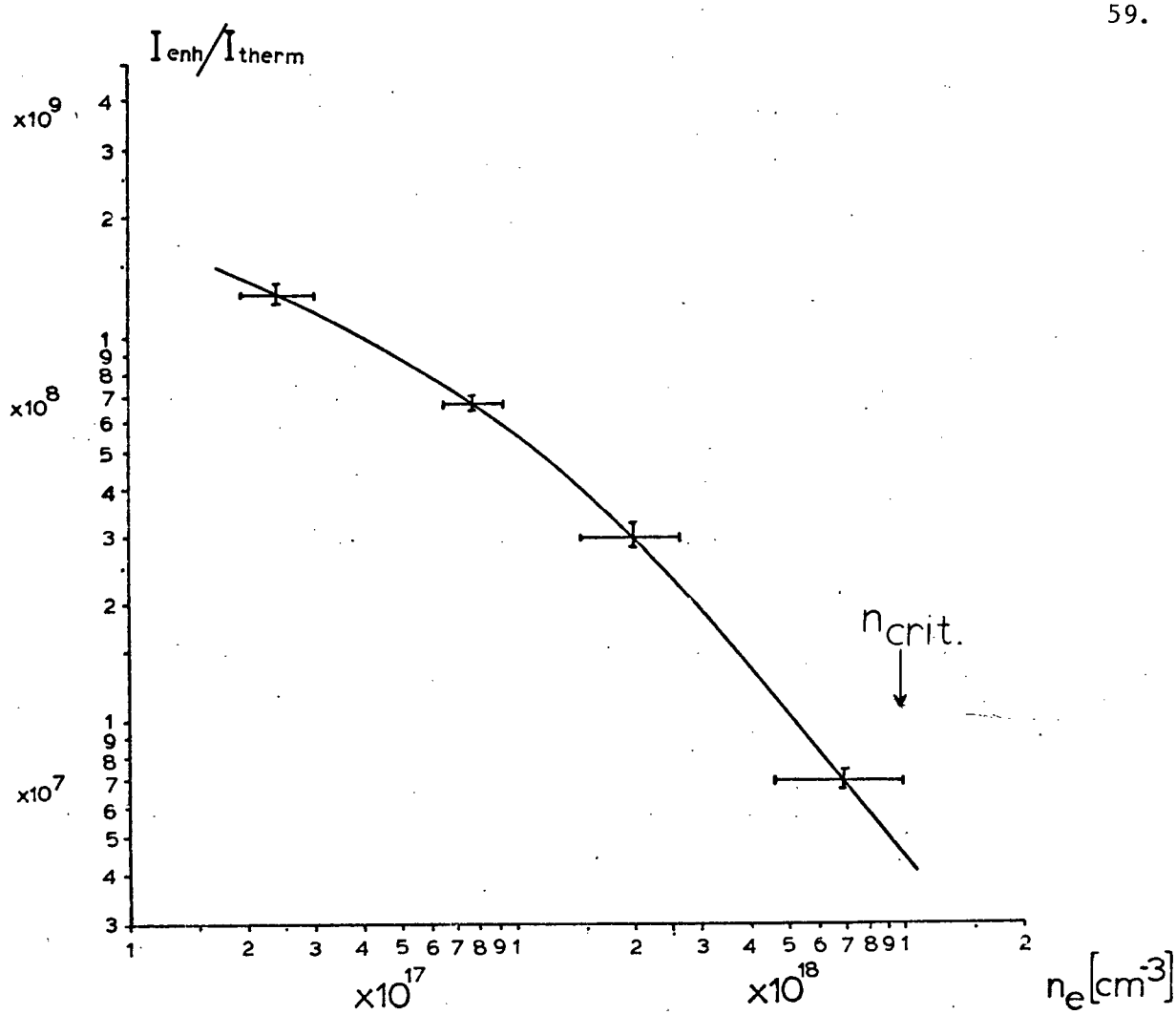

Figure (3-5): Showing the intensity enhancement above thermal levels as a function of density in the plasma. Vertical error bars are experimental errors from Fig. (2-4); horizontal error bars are due to the density estimates from Fig. (2-1).

With this information not being available at this point, the qualitative behaviour of I_{enh}/I_{therm} versus n_e could perhaps be understood by the fact that increasing density and temperature at decreasing dimensions (the plasma is pinching) means decreasing scale lengths, hence increasing thresholds.*

---

*see p.29

To calculate the density fluctuation that gives rise to this enhancement, one again needs to know the thermal fluctuation first. As is well known,[29] the relative thermal density fluctuation $\frac{\delta N_{therm}}{N}$ of N particles within a given control volume containing on the average $N >>> 1$ particles, is

$$\frac{\delta N_{therm}}{N} = \frac{\delta n^{therm}}{n} = \frac{1}{\sqrt{N}} \qquad \text{(III-9)}$$

where n denotes the corresponding particle densities.
The intensity I_{BS}^{therm} scattered from these thermal fluctuation is

$$I_{BS}^{therm} \sim \langle |\delta n^{therm}|^2 \rangle \qquad \text{(III-10)}$$

Hence, the relative intensity enhancement above thermal levels $I_{BS}^{enh}/I_{BS}^{therm}$, follows from the density fluctuation enhancement above thermal levels $\frac{\delta n^{enh}}{\delta n^{therm}}$ through

$$\frac{\delta n^{enh}}{\delta n^{therm}} = \left[\frac{I_{BS}^{enh}}{I_{BS}^{therm}}\right]^{\frac{1}{2}} \qquad \text{(III-11)}$$

This, together with (III-9) yields the absolute density fluctuation giving rise to the observed intensity enhancement as

$$\frac{\delta n^{enh}}{n} = \frac{1}{\sqrt{nV_{LP}}} \times \left[\frac{I_{BS}^{enh}}{I_{BS}^{therm}}\right]^{\frac{1}{2}} \qquad \text{(III-12)}$$

where V_{LP} is the interaction volume.
Note that $\frac{\delta n^{enh}}{n}$ depends only weakly on the interaction volume. As we discuss enhancements of several orders of magnitude, an inaccurate guess in V_{LP} by a factor 10 does not change the contents of a statement about $\frac{\delta n}{n}$.

Fig. (3-6) shows the observed $\frac{\delta n^{enh}}{n}$ as well as the theoretical $\frac{\delta n^{therm}}{n} \sim n^{-\frac{1}{2}}$.

The overall enhancement above thermal fluctuations is about four orders of magnitude.

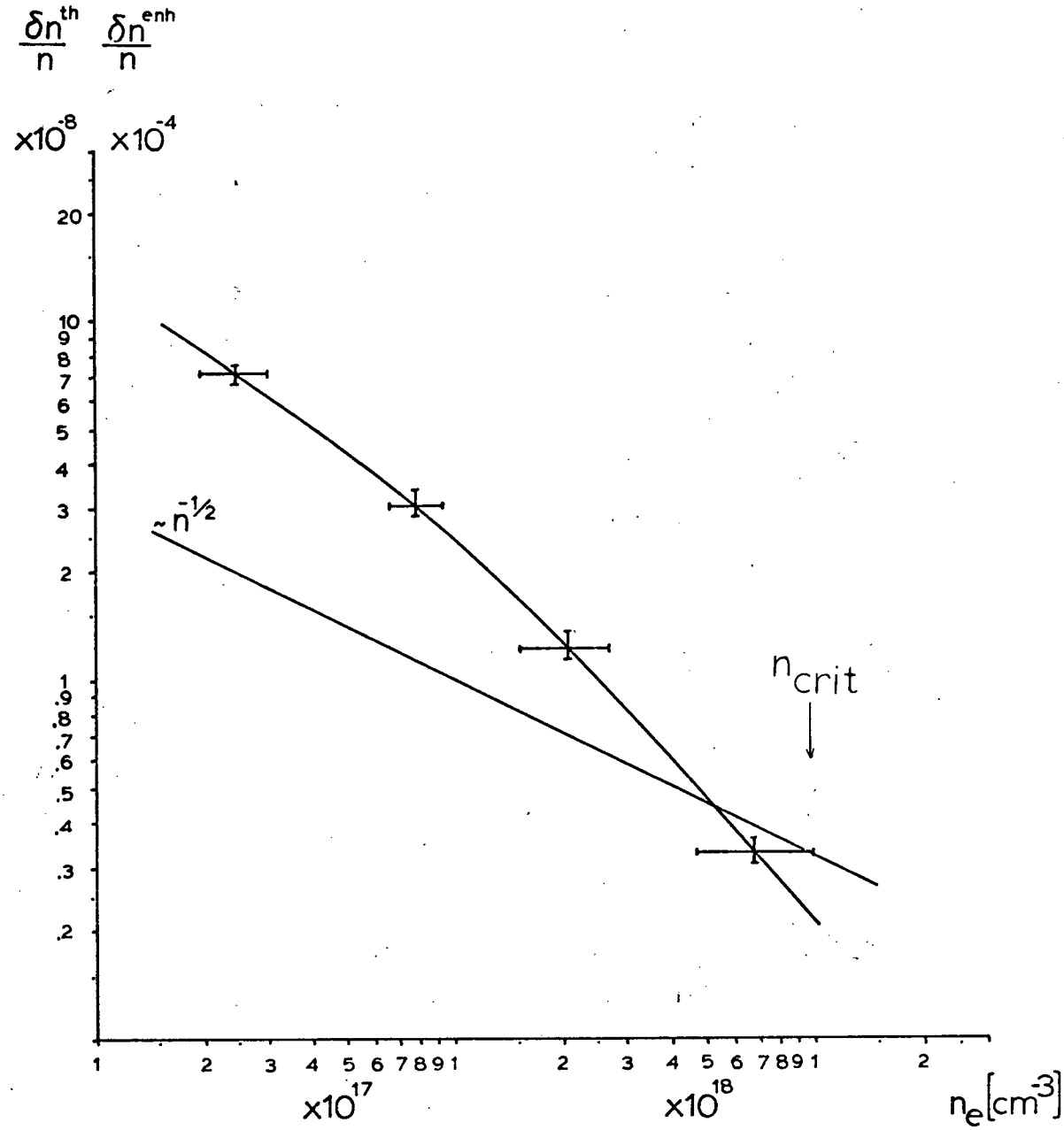

Figure (3-6): Showing the absolute density fluctuations giving rise to the enhanced backscattered light signal as a function of plasma density. Error bars like in Fig. (3-5). The straight line represents relative thermal density fluctuations.

3.22 Discussion of the observed wavelength shift of the backscattered CO_2 laser light.

The wavelength shift of the backscattered CO_2 laser light was measured, in several independent experiments, to be $(4.7 \pm .4) \times 10^{-3}$ μm towards the red end of the spectrum.

In principle, this implies a net recession velocity v_r of the reflecting object of

$$v_r = \frac{c}{2} \frac{\Delta\lambda}{\lambda_o} \qquad \text{(III-13)}$$

which for the quoted $\Delta\lambda = 4.7 \times 10^{-3}$ μm is

$$v_r = 6.6 \text{ cm/μsec.}$$

The very nature of the backscattering experiment however does not allow distinguishing between a shift arising from bulk plasma motion and a shift arising from the scattering off travelling ion acoustic waves.* Therefore, the velocity of the bulk plasma motion towards the incident CO_2 laser shall be estimated.

Then, the heating of the plasma by inverse bremsstrahlung under the given plasma parameters will be considered. From that, we try to conclude under which circumstances the enhanced backscattering of CO_2 laser light occurs.

To estimate the axial escape velocity, we proceed two ways. Momentum conservation for an infinitesimal mass element of the radially collapsing plasma shows that the axial escape velocity must be of the order of the

---

*same for other experiments of this type, e.g. 30,31.

radial collapse velocity. From streak photography* this was measured to be $\sim$ 4 cm/μsec.

Considering, on the other hand, free thermal expansion out of the ends of a plasma column (radially confined by a magnetic field), one would estimate the excape velocity to be larger or equal to the ion thermal speed which, at T $\sim$ 25 eV, is about 3.5 cm/μsec.

With both estimates leading to the same result, we assume 4 cm/μsec for the axial escape velocity v_{esc}.

Next, we combine the axial escape velocity of the plasma with the measured wavelength shift of the backscattered light to make a statement about the temperature of the region from which the enhanced backscattering occurs. Scattering off ion acoustic waves driven by the incident CO_2 laser light will result in a red shift proportional to the group velocity v_{ia} of the ion acoustic wave. If this ion acoustic wave travels in a plasma that moves as a whole towards the incident CO_2 laser light with velocity v_{esc}, the net wavelength shift due to both motions will be

$$v_{ia} - v_{esc} = \frac{c}{2}\frac{\Delta\lambda}{\lambda_o} \qquad \text{(III-14)}$$

e.g. if $v_{ia} = v_{esc}$, no shift will result.

With v_{esc} estimated as 4 cm/μsec and an observed wavelength shift of $\Delta\lambda$ of 4.67×10^{-3} μm, this is

$$v_{ia} = 10.6 \text{ cm/}\mu\text{sec}.$$

Using the dispersion relation for ion acoustic waves at equal ion and electron temperatures and taking $k\lambda_D << 1$ (see p. 57), one obtains for the temperature of the plasma in which the ion wave travels

---

*see footnote p. 33

$T = 70$ eV for $v_{esc} = 0$ cm/μsec

$T = 180$ eV for $v_{esc} = 4$ cm/μsec

Next, we proceed to make a temperature estimate from inverse bremsstrahlung considerations.

The inverse bremsstrahlung absorption* κ_B of CO_2 laser light by a plasma of $n_e \approx 2 \times 10^{18} cm^{-3}$, $T_e \approx 25$ eV, which are the parameters at the time of interest (see Fig. (2-3) middle), is found to be

$$\kappa_B = 22 \text{ cm}^{-1}$$

Hence, over 2 mm, 99% of the incident radiation would be absorbed.

Because of the finite temperature conductivity of the plasma it is unreasonable to assume such a local heating of a 17 cm long plasma column and one has to take temperature diffusion into account.

Considering the loss of thermal energy out of a volume limited by the CO_2 laser focal area and these 2 mm absorption length due to temperature diffusion only, using the thermal conductivity[19,32]

$$\kappa_T = \frac{10k_B \, (2k_B T)^{5/2}}{\pi^{3/2} m_o^{1/2} \, e^4 \ln\Lambda} \quad ** \qquad \text{(III-15)}$$

and typical assumed temperature scale lenths ℓ_T of the plasma, one arrives at a representative diffusion time τ_T of

$$\tau_T = \ell_T^2 \times 4.9 \times 10^{-22} \frac{n_e^2}{T^{5/2}} \qquad (T_{in} \text{ eV}) \qquad \text{(III-16)}$$

For scale lengths $\ell_T \sim$ mm, $n_e \approx 2 \times 10^{18} cm^{-3}$ and $T \gtrsim 20$ eV, τ_T is found to be $\lesssim 10$ nsec. As τ_T is proportional to $T^{-5/2}$, higher temperatures result in much smaller times τ_T.

---

*see (III-1)

**$\ln\Lambda \approx 10$ is the Coulomb logarithm

Hence, it must be assumed that the interaction volume V_{LP}, where the CO_2 laser energy is dumped into the plasma, is many times the 99% inverse bremsstrahlung absorption length, e.g. the entire length of the plasma column.

The energy content $E = N K_B T$ of the plasma column at $n_e \sim 2 \times 10^{18} cm^{-3}$ and $T_e \sim 25$ eV is about $E = 2.0$ Joules.

Hence, absorbing all the incident 27 Joules of laser light within the plasma leads to a $\frac{27}{2}$ fold increase in temperature or to a heating to $T_e = 350$ eV.

In applying inverse bremsstrahlung consideration however, several assumptions were made, which are in reality not fulfilled.

The derivations leading to III-1, III-3, and III-15 assume that the heating is infinitesimal, e.g., that the temperature before and after the absorption process is essentially the same, that κ_B is not a function of distance and that κ_T is neither a function of temperature nor time.

Attempts within this laboratory* to solve the exact problem numerically are under way.

Considering that the inverse bremsstrahlung absorption coefficient decreases as the plasma temperature increases and that most likely some of the incident CO_2 laser light is refracted away from the plasma[28] without being absorbed, one will have to conclude that the plasma is heated to less than 350 eV by inverse bremsstrahlung absorption. An earlier experiment[9] however with somewhat different geometry, indicated heating to 200 eV.

There exists however also the possibility that the region from where the backscattering occurs is actually a region of lower density which lies

---

*Barnard, Gulizia, private communications.

outside the main plasma body and for which the inverse bremsstrahlung absorption coefficient is lower and therefore the temperature increase due to heating by inverse bremsstrahlung absorption is also lower. The experiment discussed in 3.24 seems to support this view.

Strictly speaking, there is not yet enough experimental data to decisively conclude on the circumstances under which the observed enhanced scattering occurs but from the measurements and considerations presented it can be concluded that the enhanced scattering off ion acoustic waves (stimulated Brillouin scattering) occurs in a region in front of the main core of the plasma where the electron density is some $\sim 10^{17}$ cm^{-3}, the temperature is around 180 eV and the temperature scale lengths are of the order of millimeters. The enhancement in backscattered intensity and in induced density fluctuations above thermal levels is likely to be somewhat higher than indicated by Figs. (3-5) and (3-6).

3.23 The angular dependence of the backscattered CO_2 laser light and comparison with theory.

The angular dimensions of the setup for measuring the backscattered CO_2 laser light were as follows.

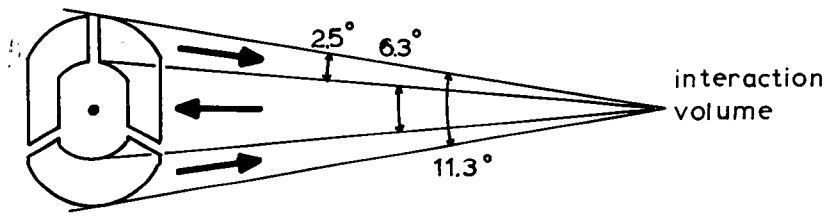

Figure (3-7): Angular dimensions of the CO_2 laser focussing optics (see also p. 34). The arrows incidate that the laser light was incident through the annular region; backscattered light was observed separately through the annular region and through the central region of the annulus. The spot in the middle indicates the area obscurred by an obstacle put in the way of the axially escaping plasma to prevent severe mechanical damage to the KCl lense.

By using appropriate masks in the backscattering optics (see Fig. (2-10) and (2-11)) and comparing the backscattered peak intensities it was found that 7.9 times more light was scattered back through the big mask as compared to the small mask (Figs. (2-12) and (2-13)). As an estimate it is therefore reasonable to say that the divergence angle of the backscattered light is about 3° to 5°.

Comparison with theory

Omitting the $\sim \cos^2\phi$ dependence predicted for the backscattered light by the theory for infinite, homogeneous plasmas as too simple, we will restrict ourselves to the comparison with two more elaborate theories predicting the typical angular divergence for Brillouin backscattered laser light.

The first theory[14] is the treatment of stimulated backscattering in a finite, inhomogeneous plasma which predicts a typical angular spread $\delta\theta_{BS}$ of (quoted in Ref. 33)

$$\delta\theta_{BS} = \frac{4}{\sqrt{\beta\ell}} \qquad \text{(III-17)}$$

There, $\beta\ell$ is the total gain observed when a backscattered electromagnetic wave travels through a medium of length ℓ with a gain of β per unit length.

The second theory[33] was forewarded recently by Lehmberg. Knowing that the first theory predicts for typical laser fusion experiments angular spreads which are far larger than observed, the second theory assumed not only that a scattered electromagnetic wave travels through a medium with gain, but also, that it has to satisfy a Bragg condition set up by the interference of different angular parts of the incident light beam in the plasma.

From that, an angular resolution for the backscattered light of

$$\theta_{min} = \left(\frac{8}{\beta\ell}\right)^{1/4} \left(\frac{\beta}{k_o}\right)^{1/2} \quad \text{is derived.} \qquad \text{(III-18)}$$

Here, k_o is the wave vector of the incident light.

The predictions of both theories for a typical laser fusion experiment on one hand, and the experiment described in this report on the other hand, will now be compared.

Typical laser fusion experiment[33]	parameters	This experiment
k_o(Nd glass) = 6 x 10^4/cm		k_o(CO_2 laser) = 6 x 10^3/cm
$\beta\ell$ 10 to 15		$\beta\ell$ 19 *
ℓ 100 μm		ℓ 5 mm
β (1 to 1.5) x 10^3/cm		β 38/cm

*see Fig. (3-5)

Typical laser fusion experiment	This experiment
Theoretical Predictions	
$\delta\theta_{BS} \sim 1.2$ or 60°	$\delta\theta_{BS} \sim .93$ or 53°
$\theta_{D\ min} \sim .14$ or 8°	$\theta_{D\ min} \sim .063$ or 3.6°
Observed	
$\sim 3^{\circ}$	$\sim 3^{\circ}$

It is clear that the first theory fails in explaining both types of experiments. The experimental evidence suggests the correctness of Lehmberg's formula.*

---

*The author wishes to emphasize that even though he claims to understand the physical principle behind III-18 as it is described in Ref. 33, he would at this point be unable to rederive III-18 from first principles. The description of the results obtained in Ref. 33 is however explicit enough that numerical values can be obtained from the presented formulae.

3.24 The wavelength dependence of the light backscattered through the small mask *

The experimental result (Fig. (2-13)) shows that the spectrum of the CO_2 laser light scattered back through the small mask is not simply a line shifted by 4.7×10^{-3} μm

The center of the line is still shifted by 4.7×10^{-3} μm but additionally wings are present, suggesting a modulation frequency ω_M of

$$\omega_M \sim (3.5 \text{ to } 2.9) \times 10^{10} \frac{\text{rads}}{\text{sec}}$$

To my knowledge, the angular dependence of stimulated Brillouin scattering has not been measured before with this type of geometry (see Fig. (3-7)) and such a modulation has not yet been observed. Note that this modulation frequency is now an absolutely determined frequency that is not obscured by any immeasurable shifts due to bulk motions, etc.

In trying to provide a physical explanation it was found that the modulation could best be explained through the gyration of electrons in the pinch magnetic field. The necessary reasoning shall now be presented.

For a scattered spectrum to be modulated, a nonlinear coupling between the modulation oscillation and the oscillation of the scattering electron in the electromagnetic fields must exist.

In a stationary magnetic field, the Lorentz force provides this coupling in a very natural way by simply modulating the velocity of the electron with the gyro frequency ω_g where

---

*see 2.6

$$\omega_g = \frac{eB}{m} \qquad \text{(III-19)}$$

For these modulations to be visible however, the wave vector of the density fluctuation scattering the incident electromagnetic wave must be very near perpendicular to the vector of the magnetic field[48,52] (e.g. $< 5^o$). Otherwise, the thermal motion of electrons moving parallel to the magnetic field produces enough Doppler broadening to smear out the modulations. Considering the setup in Fig. (2-10) and the angular dimensions of the focussing and backscattering optics (Fig. (3-7)), one can see that this requirement is fulfilled.

Secondly, the spectrum of thermal electron density fluctuations perpendicular to an applied magnetic field already shows modulations at multiples of the electron cyclotron frequency.

Thirdly, it will be seen that no other characteristic frequency in a plasma of a density of $2 \times 10^{18} cm^{-3}$ is in the vicinity of the observed modulation frequency.

In order to support these statements, we will first use (III-19) to calculate the magnitude of the magnetic field at the interaction volume. Then we will estimate this magnitude from plasma dynamic considerations. The observed spectrum (Fig. (2-13)) suggests a modulation frequency of

$$\omega_M = (3.2 \pm .6) \times 10^{10} \frac{\text{rads}}{\text{sec}} \; *$$

Setting this equal to the gyro frequency ω_g and using (III-19), this suggests a magnetic field at the interaction volume of

B 2000 Gauss

The magnitude of this magnetic field will now also be estimated from the current flow and the size of the interaction volume in the plasma,

*The lower limit of ω_M is hard to estimate as the observed frequency modulation is at the limit of what can be spectrally resolved.

applying the theory of the skin effect in uniform cylindrical conductors.

As this theory is presented in almost any test book on electrodynamics*, it will not be presented here to any extent, only its results will be used.

Current traces of the Z-pinch discharge** show the magnitude of the current flowing through the plasma to vary on a time scale of $\sim$ 1 μsec, e.g. with a frequency of

$$\omega_I = 2\pi \times 10^6 \frac{\text{rads}}{\text{sec}}$$

Assuming that the plasma is a uniform conductor of radius r_o = 2 mm*** with a temperature of 180 eV†, its resistivity σ†† will be

$$\sigma \approx 4 \times 10^{-5}\ \Omega\ \text{cm}$$

or that of a metal. From that one can calculate a skin depth

$$\delta = \frac{c}{\sqrt{2\pi\omega_I\sigma}} \qquad \text{(c = speed of light)} \qquad \text{(III-20)}$$

of δ = .33 mm.

As the radius of the plasma is r_o = 2 mm, one can see that the majority of the current flow occurs at radii larger than the radius of the back-scattering interaction volume (r ≈ .5 mm).

Applying the results of the skin effect theory for a uniform cylindrical conductor with outer radius r_o = 2mm and a current skin depth of δ = .33 mm, one finds that the current flowing through a central part

---

*see particularly 49,50

**see specification.

***see p.32

†see p. 66

††see p.26

with r = .5 mm is

6.7×10^{-3} of the total current.

With the total current measured to be 110 k amps at the time the back-scattering takes place, this means that the current flowing through a circular cross-section with a radius equal to that of the focal spot is

740 amps.

To calculate the magnetic field surrounding this current, one uses Stokes theorem to evaluate Maxwell's equation $\nabla \times \vec{H} = \vec{j}$ for the given geometry to obtain

$$B(r) = \frac{\mu_o}{2\pi r} I^* \qquad \text{(III-21)}$$

For r = .5 mm and I = 740 amps this results in a magnetic field B of

B = 3000 Gauss

In view of the approximations made, this compares well with the measured value (p. 71).

The approximations made were the following:

(1) The plasma was considered a uniform cylindrical conductor of r_o = 2 mm; in reality however it has a radial temperature profile, hence, a radial conductivity profile. For the assumption to hold, the temperature profile must be reasonably flat within the central region of the plasma.

---

*For the convenience of measuring I in amps, this formula is given in MKSA units. $\frac{\mu_o}{2\pi} = 2.0 \times 10^{-7} \frac{\text{Vsec}}{\text{Am}}$

(2) The scattering volume was considered a thin annular ring with $r = .5$ mm. Considering that the aperture through which the CO_2 laser light enters the plasma is an annulus already and that ray bending in the radial density profile of the plasma is likely to change the aspect ratio of this annulus to values closer to 1, the assumption made seems reasonable and is as well supported by evidence from shadow photographs (Fig. (3-2)).

Finally, we shall show that at the density of $n_e = 2 \times 10^{18}$ cm^{-3}, which is the density at the pinch time of interest, no other characteristic frequency of the plasma* is near the observed modulation frequency of $\omega_m = 3 \times 10^{10} \frac{\text{rads}}{\text{sec}}$.

(1) electron plasma frequency: $\omega_{pe} = 8 \times 10^{13} \frac{\text{rads}}{\text{sec}}$

(2) ion plasma frequency (He ions) $\omega_{pi} = 1.8 \times 10^{12} \frac{\text{rads}}{\text{sec}}$

(3) electron gyro frequency ω_{ge} for 3000 Gauss

$$\omega_{ge} = 3 \times 10^{10} \frac{\text{rads}}{\text{sec}}$$

(4) ion gyro frequency ω_{gi} for 3000 Gauss

$$\omega_{gi} = 1.4 \times 10^{7} \frac{\text{rads}}{\text{sec}}$$

(5) resonance frequency of electron waves in a magnetic field, the upper hybrid frequency

$$\omega_{uh} = \sqrt{\omega_{pe}^2 + \omega_{ge}^2} > \omega_{pe}$$

(6) resonance frequency of ion waves in a magnetic field

$$\omega_{ih} = \sqrt{k_i^2 v_{ia}^2 + \omega_{gi}^2} \quad ; \quad \omega_{gi}^2 << k_i^2 v_{ia}^2$$

*These frequencies are explained in any plasma physics book (16-19).

(6) continued

Here, $\sqrt{k_i^2 v_{ia}^2}$ is the ion acoustic frequency discussed in Section 3.22.

Hence, ω_{ih} is very close to the ion acoustic frequency (within 10^{-2}%).

(7) If an electrostatic ion wave travels exactly perpendicular to a magnetic field, it has a resonance at the lower hybrid frequency.

$$\omega_{lh} = \sqrt{\omega_{ge}\omega_{gi}} = 5 \times 10^8 \frac{\text{rads}}{\text{sec}}$$

It needs to be emphasized that the arguments presented are not meant to be unique statements about the physical process giving rise to the observed spectral intensity modulations. They rather are initial suggestions based on the available experimental data. More experiments, e.g. backscattering of CO_2 laser light at different currents in the pinch and a genuine theoretical treatment would be needed to interpret the described data conclusively.

Within the scope of the data and the reasoning presented however, it can be suggested that the observed modulation in the backscattered spectrum is most likely due to the gyration of electrons in the magnetic field of the pinch.

CONCLUSIONS

The experiments described in Chapter II and evaluated in Chapter III showed which processes can be observed when a 250 MW CO_2 laser interacts with a plasma at densities from 10^{17} cm^{-3} to some 10^{18} cm^{-3}. At low densities, the good agreement between theory and experiment shows that significant absorption of CO_2 laser light by inverse bremmstrahlung takes place. At higher densities, stimulated Brillouin scattering is seen to occur, however, at levels well below saturation[46]. The observed angular divergence of light backscattered by stimulated Brillouin scattering was seen to agree well with theoretical predictions.[33] Finally, it has been observed that some of the Brillouin backscattered light is modulated with the gyro frequency of electrons in the magnetic field in the plasma, an effect that could be of great interest for the investigation of magnetic fields in laser fusion plasmas.[35-37,49]

As far as other instabilities[14,15] are concerned, we feel that the power available with the CO_2 laser was too low to exceed their thresholds. Higher CO_2 laser powers would make it considerably easier to measure how the observed intensity enhancement of the backscattered light varies as a function of the incident CO_2 laser power.

It would also allow the imaging of the backscattering region on "footprint" paper and thus obtain direct information about the geometry of the interaction volume.

From simple, experimentally verified theories about filamentation[24,25] it can be predicted that, with the parameters described in Chapter III, a density depression of $\sim$ 3% should result. With ten times higher CO_2 laser power, this density depression will become several tens of percent, hence, should easily be observable.

Higher CO_2 laser powers would also provide a possibility of making a contribution to the question of stimulated Raman scattering. Much predicted[10,11,12,14,15] but perhaps only once observed,[22] our experiment would provide interesting density scale lengths for testing the predictions.

Appropriate changes in the discharge bank of the Z-pinch would allow the measuring of the spectrum of the backscattered light at different plasma currents, e.g. different magnetic field strengths within the laser-plasma interaction region. This would make it possible to further test if the model assumed in 3.24 is correct.

Finally, a change in geometry, e.g. focussing the CO_2 laser radially into the plasma, will have the advantage of a better defined interaction region and will allow diagnostic access to investigate two plasmon decay.[21,23]

CHAPTER 4

The fast gating of an Optical Multichannel Analyser (OMA) and a contribution to the diagnostics of the Z-pinch plasma

4.1 Introduction

The first measurements of electron density and temperature of the Z-pinch plasma were spectroscopical measurements using the Stark broadening of the 4686Å line of He II.[26]

In order to have these measurements supplemented by a second method, a Thomson scattering system (see Fig. (4-1)) was set up. A 3 Joule Ruby laser was focussed into the plasma and the backscattered light observed under 173°. At the density and temperature indicated by the initial spectroscopical measurements, this should have resulted in a Thomson-scattered spectrum characterized by $\alpha_e \approx 1.2$.

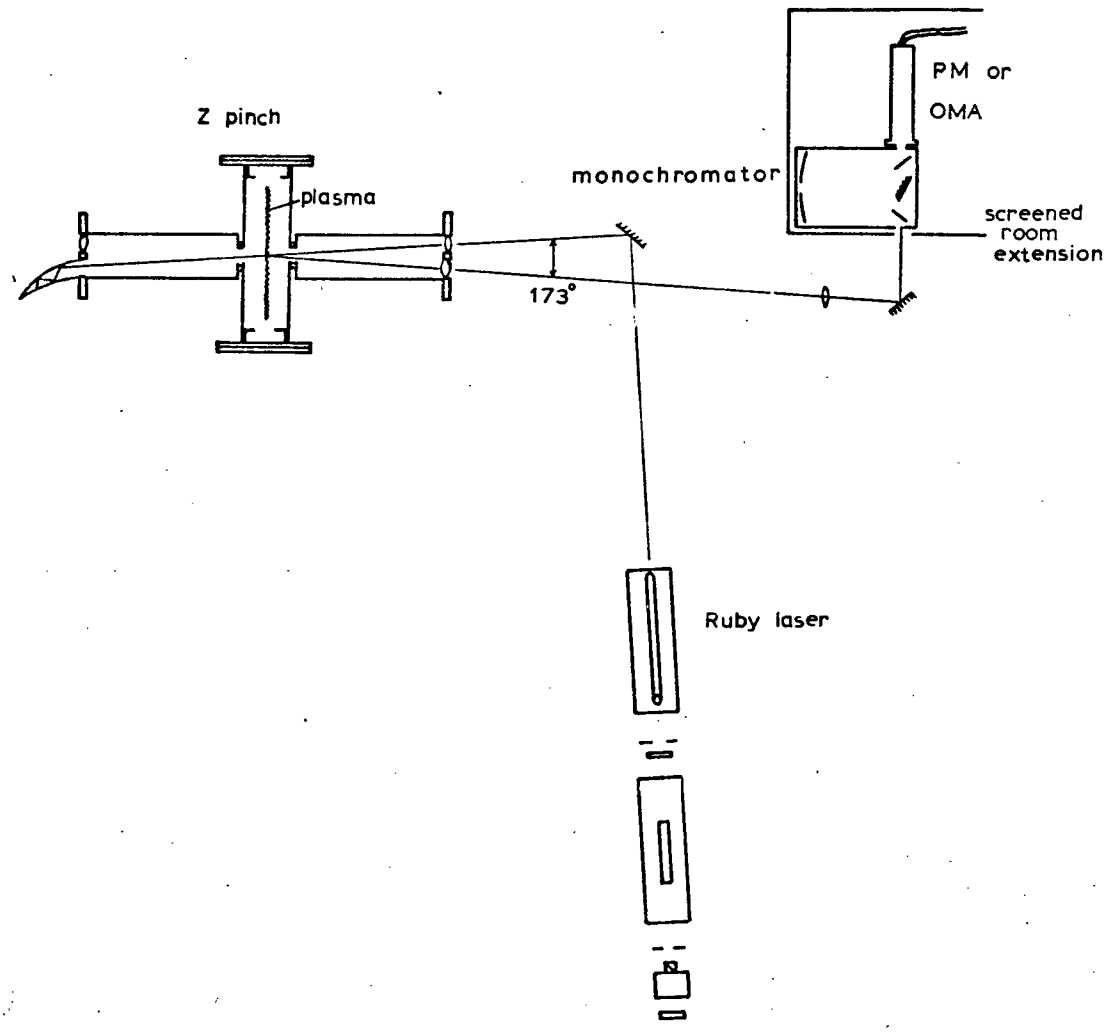

Figure (4-1): The Ruby laser Thomson scattering system.

The spectrum, obtained on a shot-to-shot basis and recorded with a photomultiplier, is shown below and yields

$$n_e \approx 10^{18}\ cm^{-3} \quad , \quad T_e = 40\ eV$$

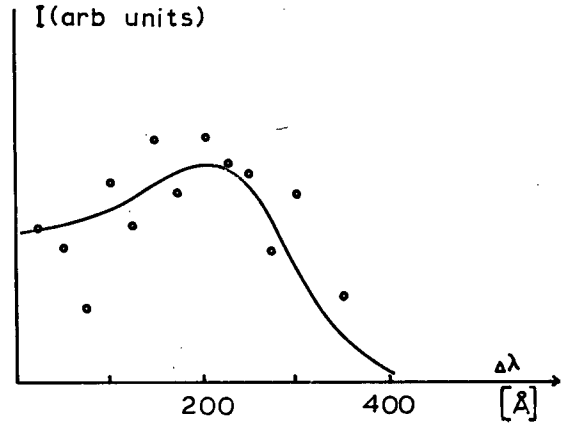

Figure (4-2): Thomson scattered spectrum obtained with setup in Fig. (4-1), recorded with a photomultiplier.

The next step was to use a 500 channel OMA in order to detect this electron feature in one single shot.

Despite much effort invested to arrive at a truly satisfactory result, this was not achieved within the work described in this report. Part of the reason can be understood by examining Figure (4-3) which shows a Thomson scattered signal detected with a photomultiplier.

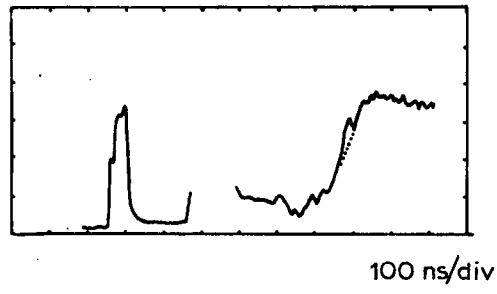

Figure (4-3): A photomultiplier trace of the Thomson scattered signal. The first pulse is the Ruby monitor. The missing piece indicates the place of a foreward scattered signal which is well off the screen and of no relevance here. The subsequent rise is the delayed signal showing the plasma light with the backscattered signal indicated. $\Delta\lambda$ was 100Å; pinchtime was $-50 < t < 0$ ns.

The Figure shows clearly that the signal-to-pinchlight ratio is about .2 or smaller. This also gives rise to the large stray of data points in Fig. (4-2).

With the means available at the time, it was found that the evaluation of the ion feature of the Thomson scattered spectrum provided a very good measurement of plasma density and temperature,* hence, the electron feature approach was not pursued any further.

The work however did result in developing a technique for successful nanosecond gating of the OMA.[40]

In the following section this technique shall be described and applied to improved spectroscopical measurement of density and temperature of the plasma.

---

*see footnote p. 33

4.2 Nanosecond gating of an optical multichannel analyser (OMA)*

Many types of time-resolved measurements in plasma physics require short time gating of a detection system during comparatively long duration high light levels. One such case is the detection of a Thomson scattered signal of nsec duration during the high bremsstrahlung emission of a dense plasma lasting many μsec.

If the detected signals are weak, two requirements must be fulfilled: The contrast ratio of the gating system must be high (e.g. > 10,000) and the gating process must not result in distortions of the recorded signal. How the OMA can be made to fulfill both conditions will now be described.

An OMA can be used in two modes of operation. In the continuous mode (also called "real time" mode), the 500 channels of the OMA are scanned every 32 msec with an open time of 768 μsec between scans. In this mode, the OMA can store about 5,000 counts per channel, each count corresponding to ∿ 20 visible photons.

In the gated mode, the 500 channels are sensitised during a desired time interval, which must be shorter than and within the 768 μsec open time. Gating is achieved by holding the photocathode of the image intensifier at ∿ 7 kV. A gating pulse of 1.1 kV to 1.4 kV brings the voltage of the photocathode up to the ∿ 8.2 kV required for full sensitivity. The manufacturer claims that gating times as short as 10 nsec are possible, but it will be shown that this is only the case if the signal received within the gating time is shorter than 10 nsec. Otherwise, very severe

---

*see specifications

distortions will result.

In order to test the response of the OMA detector under various conditions, the following experiment was set up

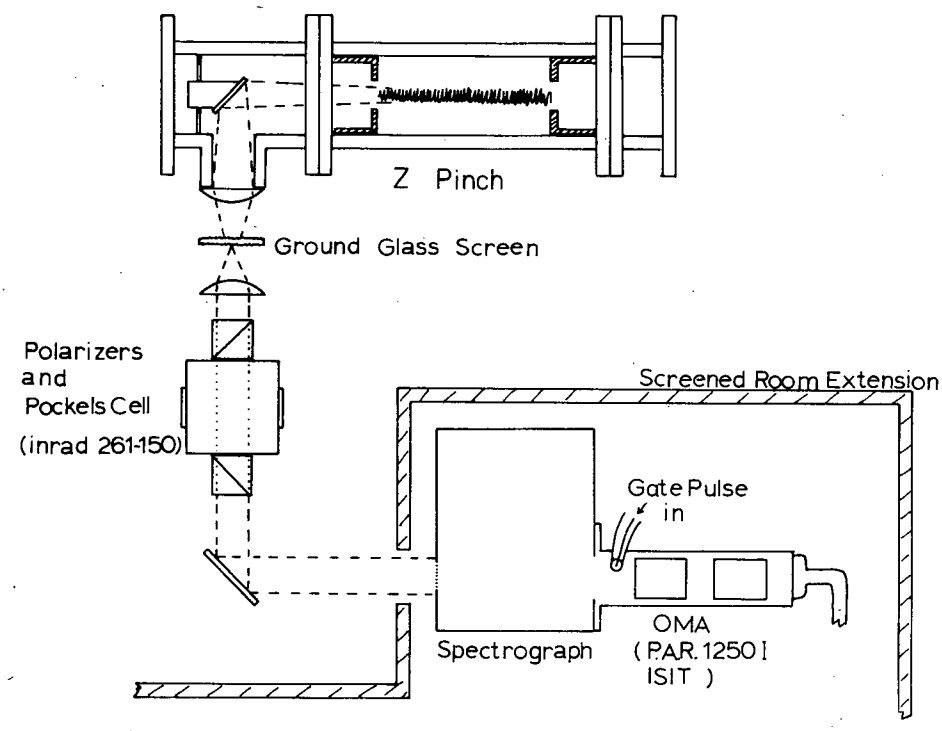

Figure (4-4): Experimental setup to test the response of the OMA in gated mode. The spectrograph is set to zero order to eliminate spectral dependences.

The Z-pinch serves as a white light source of μsec duration. The detector is mounted in the focal plane of a monochromator set to zero order to transmit white light. On the entrance slit plane a package consisting of 10 slits (25 thou wide, 25 thou apart) is mounted.* The white light image of this slit package is registered by the detector.

---

* such a slit package was already used by (26) to optimize the gating voltage.

Fig. (4-5) shows the response when the detector operates in the real time mode. The resolution is about 7 channels; the intensity response across the 500 channels is reasonably flat. Deficiencies are due to pincushion distortion.*

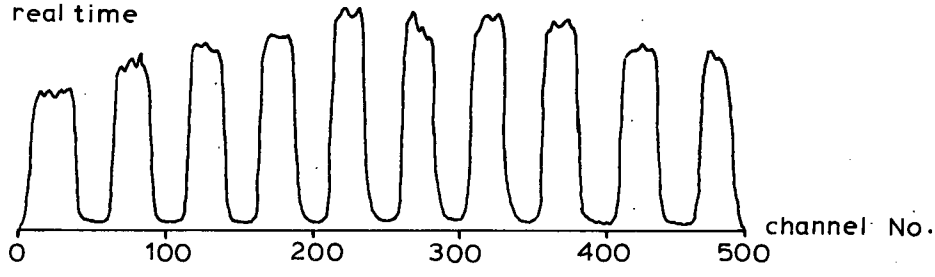

Figure (4-5): Response of the OMA in real time.

Fig. (4-6) shows the response in gated mode at long gating times. The gating was done electronically only; the gating time was 1.2 μsec. It is seen that some resolution is lost and a stretching of the spectrum across the channels occurs. These distortions, however, are minor and, as they are largely intensity independent, can be accounted for.

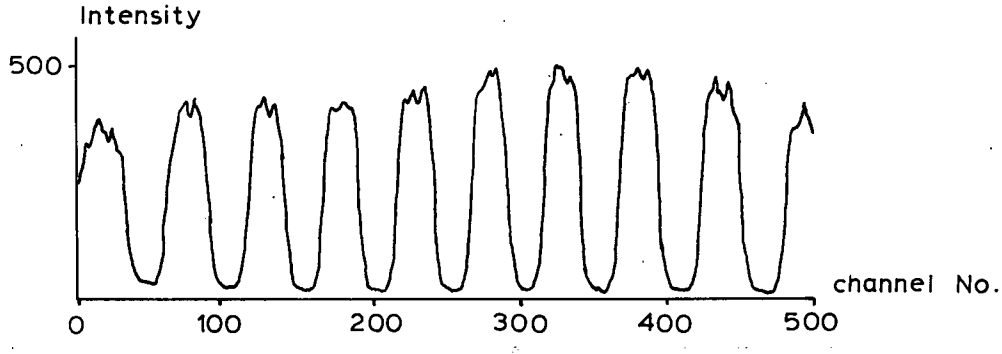

Figure (4-6): Response of the OMA when electronically gated with 1.2 μsec.

---

*I am indebted to W. Seka for information about work that has been done with OMAs at the U. of Rochester Laboratory for Laser Energetics.

Fig. (4-7) and Fig. (4-8) show the response when the gating time is 50 nsec and 6 nsec respectively.

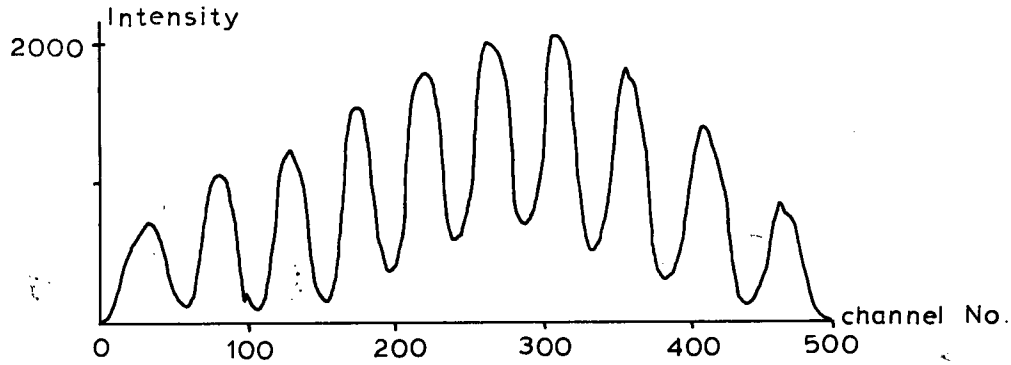

Figure (4-7): Response of the OMA when electronically gated with 50 nsec.

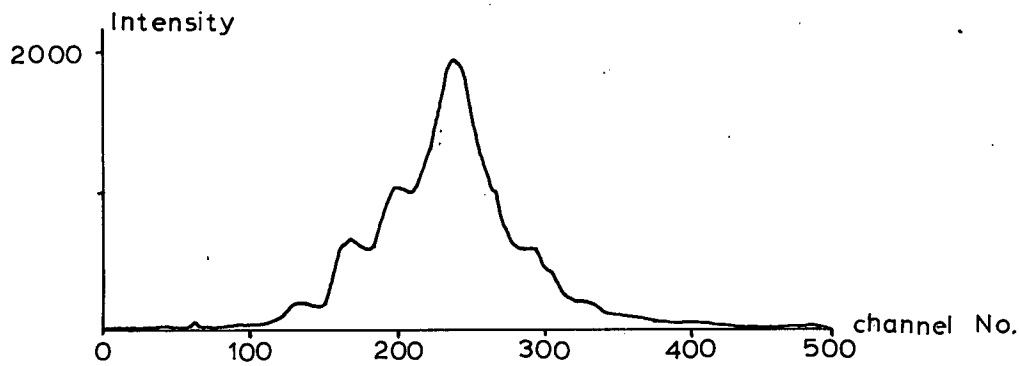

Figure (4-8): Response of the OMA when electronically gated with 6 nsec.

The distortions for 50 nsec gating time are obviously severe and for 6 nsec gating time the detector becomes useless.

These distortions are presumably caused by an incorrect and time-varying voltage applied to the photocathode[42] during the switch on and switch off of the gating pulse.

First it was tried to improve the operation of the OMA in gated mode by improving the electronics of the gating circuitry as suggested by in (45).

Additionally, the cable carrying the HV gating pulse to the photocathode of the first intensifier was removed from inside the OMA and fed directly into the OMA head termination (see 4-4).

It, however, soon was evident that the remedy could not readily be achieved by electronical means only.

To gate the incoming light with an electro-optical switch rather than gating the OMA electronically eliminated the distortions in the recorded spectrum, but careful measurements showed that a contrast ratio of about 400:1 was the best that could be achieved with this method.

To combine the advantages of both methods, i.e. the distortion free gating by switching the incoming light and the good contrast obtained by gating the OMA electronically, the following experimental setup was used.

In order to let the light signal reach the detector only during the time when the electronical gating pulse voltage is constant, an optical gating pulse (30 nsec) was fitted temporally into a 50 nsec electronic gating pulse. The voltage of the electronic gating pulse was adjusted to give the least distortions across the whole spectrum at long gating times. The timing of the two pulses can be done with synchronized cable discharges.

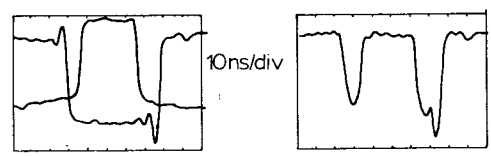

Figure (4-9): Electronical and optical gating pulse temporally fitted into each other. Pulse height is 1.2 kV.

Fig. (4-9) shows that during the time the optical gating pulse is switched, the voltage of the electronic gating pulse is quite stable.

Fig. (4-10) shows again the real time response of the OMA, but the setup (Fig. (4-4)) now includes the Pockels cell. The intensity distribution across the spectrum now arises mainly from the fact that the open aperture of the Pockels cell (= 15 mm) was only slightly larger than the sensitive area of the OMA.

Fig. (4-11) shows the performance of the OMA in gated mode for both gating pulses combined.

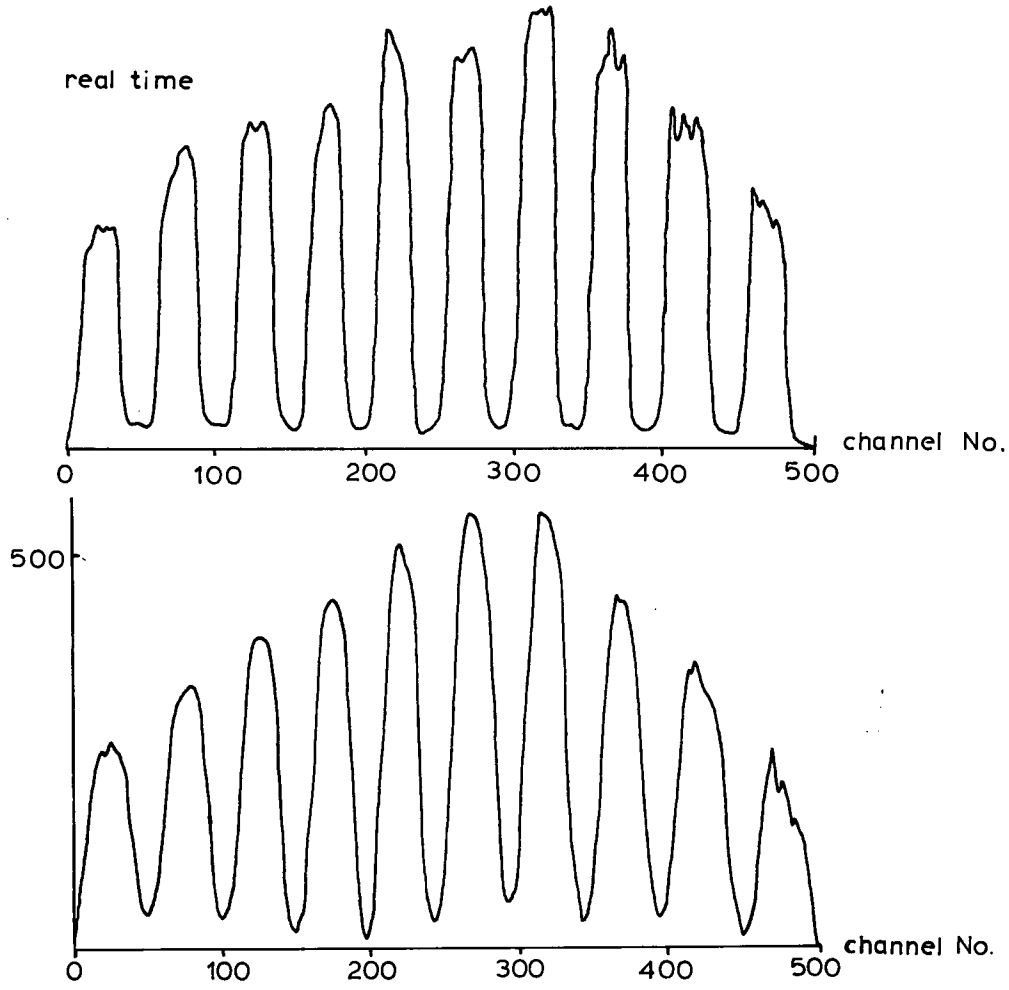

Figures (4-10) and (4-11): Response of the OMA (a) in real time (b) for the identical setup when electronically gated with 50 nsec and optically gated with 30 nsec.

The absence of any background such as in Fig. (4-7) is immediately obvious. The intensity distribution of the real time spectrum is closely reproduced. Fig. (4-12) shows that the resolution in this double gating mode is improved as compared to the electronical gating only.

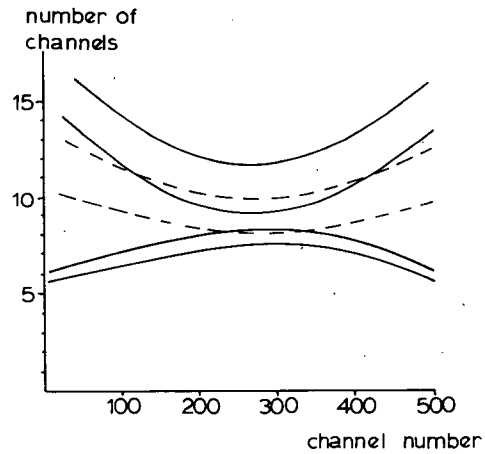

Figure (4-12): A comparison of the focusing properties for the investigated cases. The number of channels on the rise and fall of the slit image is shown as a function of channel number for the three cases. The upper solid curve shows the electronically gated mode, the lower solid curves shows the real time behaviour and the dashed one shows the results from the combined gating pulses.

It finally was observed that in the gated mode, the intensity sensitivity of the OMA is only linear up to at most $\sim$ 2000 counts/channel. This is illustrated in Fig. (4-13).

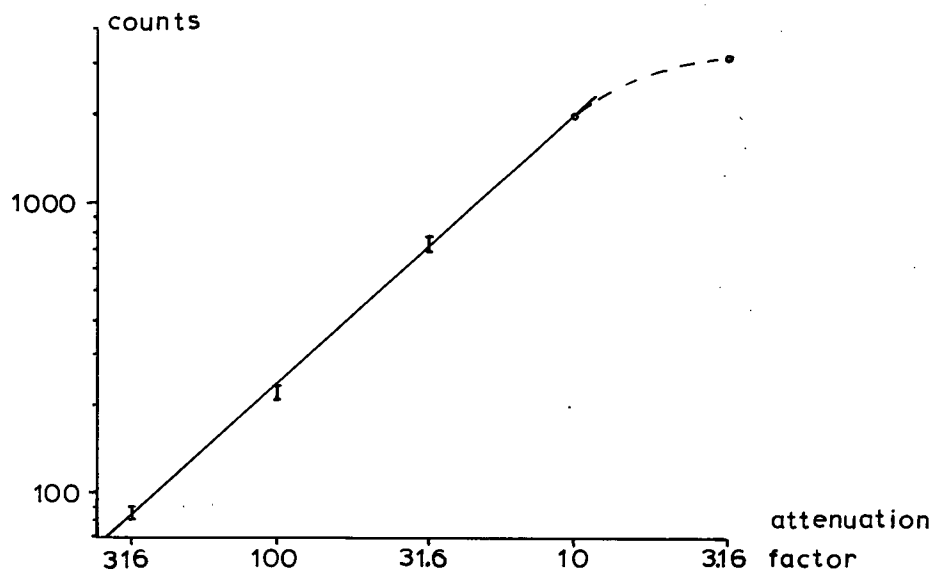

Figure (4-13): Shown are the number of counts in a given channel as a function of intensity. The intensity was varied by inserting filters of increasing neutral density in the light path between the source and the OMA (see Fig. (4-4)).

From the measurements presented, the following conclusions can be drawn. The background observed in the spectrum when the OMA is gated electronically only (Fig. (4-7)) arises from leakage of photocurrent due to light reaching the detector when only 7 kV are applied. The distortion in the intensity distribution is indeed due to the switchon and switchoff process with light falling on the OMA sensitive elements as suggested by (42). The advantages of the double gating technique are, apart from removing the difficulties mentioned above, that:

The contrast requirements for the optical gate are not any more determined by the time the light source is active, but by the electronic gating time. Hence, to achieve faster gating times, only the optical gating pulse needs to be shortened.

The quality requirements (e.g., squareness) for the electronic (as well as optical) gating pulse are much relaxed, as long as the voltage is steady during the switching time of the optical gate. This completely eliminates the need for elaborate gating circuits.

4.3 Spectroscopic measurements of plasma density and temperature using the 4686Å line of He II.

The double gating technique described in 4.2 will now be applied to spectroscopic temperature and density measurements using the 4686Å line of He II. Even though this type of diagnostics had already been used,* improved measurement appeared desirable. Fig. (4-14) shows, as an example, the 4686Å profile at pinch time t = + 300 nsec, composed of five separate measurements.

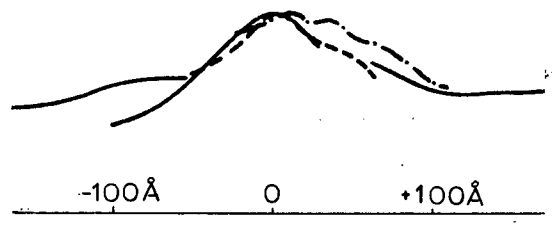

Figure (4-14): Data of earlier spectroscopical measurements
Composed line profile at 4686Å at t = + 300 nsec.

Despite excellent experimental work, the means available at that time simply did not allow better data to be obtained.

---

*26

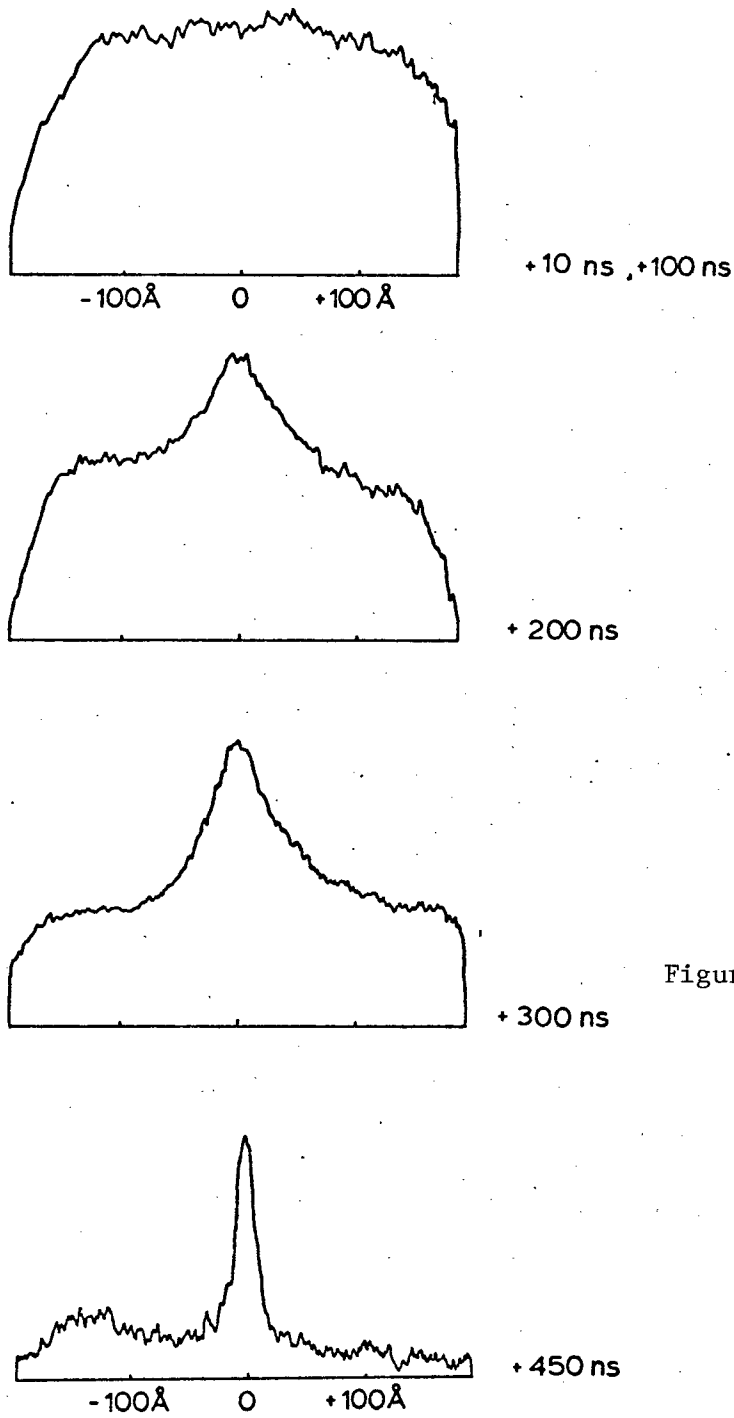

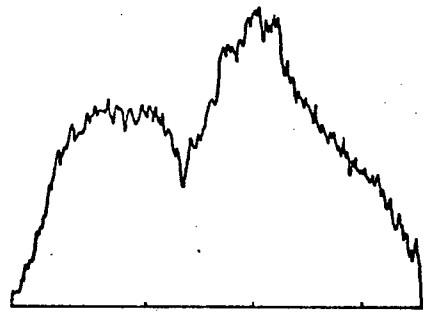

Figure (4-15):
Left Row: 4686Å profiles obtained with double gating technique (see 4.2),
Right picture: 50 nsec electronic gate only, also at t = 200 nsec.

Fig. (4-15) shows a selection of 4686Å profiles obtained with the double gating technique (30 nsec optical, 50 nsec electrical) and a monochromator of less dispersion than used previously.[26] The experimental setup was essentially the same as shown in Fig. (4-4), of course without ground glass screen, and the plasma was viewed side on.

As a comparison, the right picture in Fig. (4-15) shows the result obtained with 50 nsec electronical gating only. It must be emphasized that the OMA used by Houtman[26] had only one image intensifier. The OMA employed in the measurements described here had two image intensifiers which resulted in more severe distortions when the OMA was gated electronically only.

Evaluating the width of these lines to obtain the electron density and the total line to continuum intensity ratio to obtain the electron temperature[43,44] of the plasma at a given time, one obtains the data shown in Fig. (2-1) which agree well with the ion feature Thomson scattering measurements, as far as the density is concerned. As for the temperatures, the theories allowing the determination of temperature from the line to continuum ratio of intensities $(\frac{L}{C})$ are too uncertain for ratios $\lesssim 1$.*

This, and the disappearance of the 4686Å line at higher temperature due to a decrease in the amount of HeII ion present, does not allow for a good temperature measurement at pinch times of interest.

---

*for $\frac{L}{C} \approx 1$, at densities of $\sim 5 \times 10^{18}$, (46) predicts about 40 eV, (47) predicts about 5 eV.

Specifications

(1) Z-pinch

Details of the Z-pinch are described in Ref. 26 . Here, only the most important characteristics shall be described.

He - filling pressure	1.2 Torr
inner radius vessel	5.08 cm
outer radius vessel	5.72 cm
material of vessel	pyrex
Electrode separation (copper)	35.6 cm
Bank capacitance	84 μF
Bank inductance	33 n H
Bank energy at 11.5 kV charging voltage	5.6 kJ
Typical maximum current of discharge	150 k Amp
Time of maximum density and temperature	2.0 μs after initial breakdown

Figure (5-1): Shows the circuitry of the Z-pinch discharge bank. Note the added preionization discharge at the anode, mentioned in 2.2.

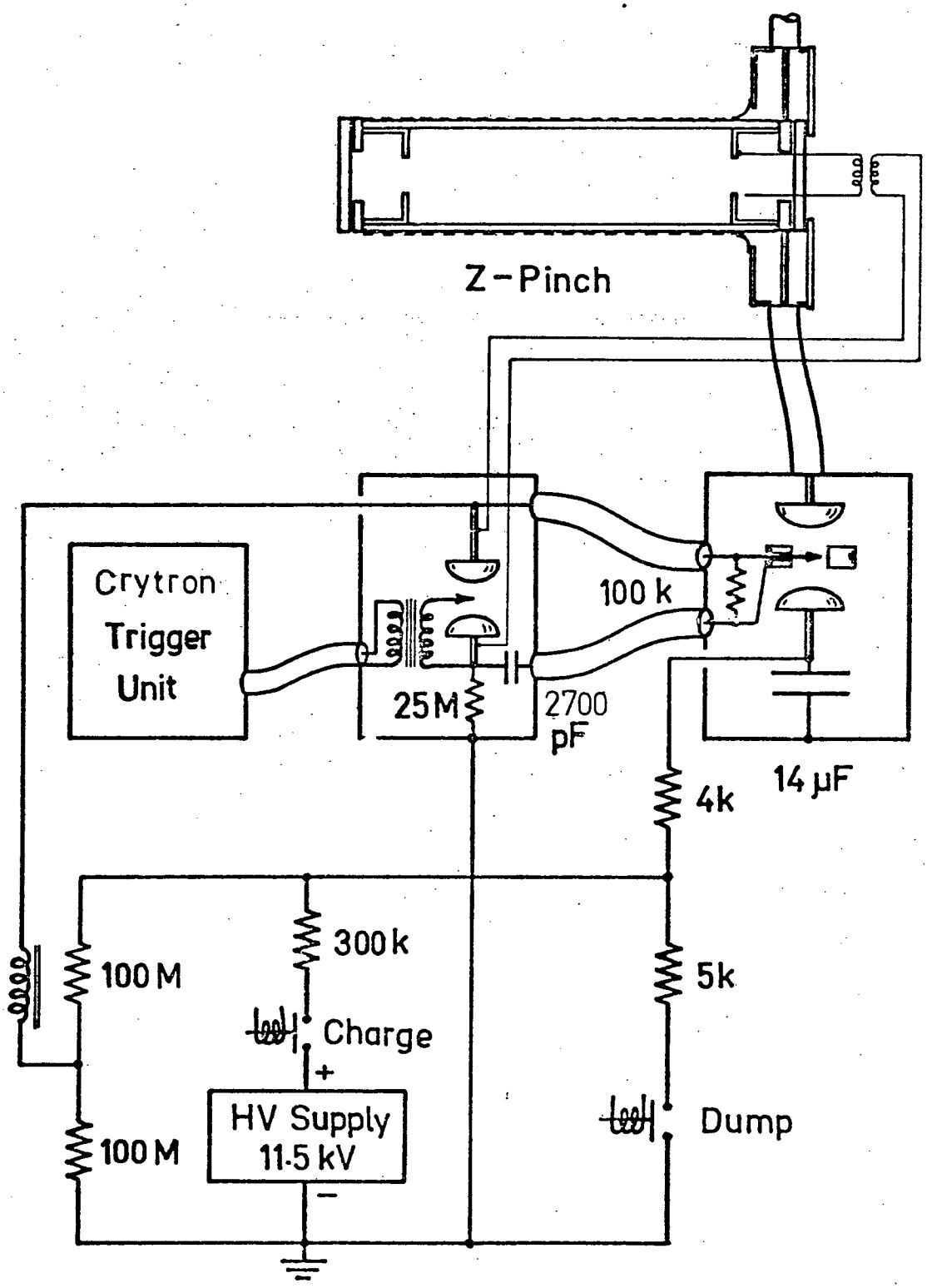

A typical $\frac{dI}{dt}$ trace as picked up by the Rogowsky coil is shown in the figure below. Maximum current I = 180 k amp.

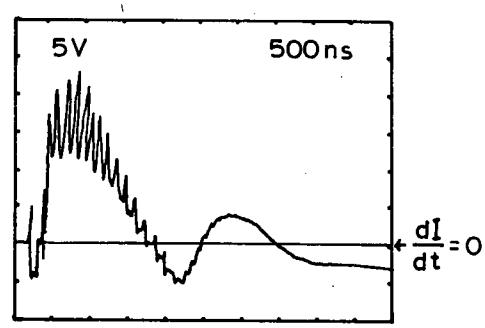

Figure (5-2): $\frac{dI}{dt}$ as a function of time; Rogowsky coil signal.

(2) CO_2 laser

Type: Lumonix T600

Cavity: unstable resonator configuration

Output geometry: see Figs. (2-1) and (2-2).

Typical output pulses at an energy of 27 Joules is shown in the section (3) Detectors.

(3) Detectors

Au Ge: Gold doped germanium semiconductor detector, liquid nitrogen cooled, sensitive for $\lambda < 11\ \mu$.

Calibrated sensitivity at 10.6 μ is 6.7 V/mJ.

Sensitive area 16 mm^2.

Fig. (5-3) shows the CO_2 laser pulse as registered by the Au Ge detector.

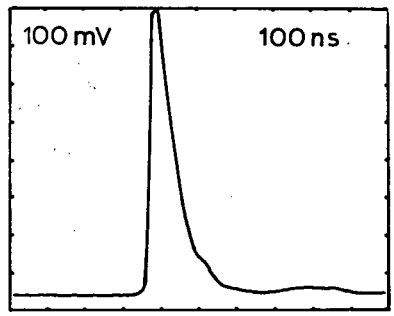

Figure (5-3): CO_2 laser pulse, Au Ge detector.

<u>Pyro electric detector:</u> Molectron Corp Model P3-00

50% of maximum sensitivity for $\lambda > 8\ \mu$.

Calibrated sensitivity at 10.6 μ is better than 1.5 V/mJ.

Sensitive area 1 mm^2.

Fig. (5-4) shows the CO_2 laser pulse as registered by the Pyro electric detector.

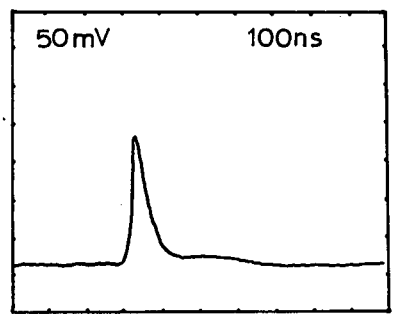

Figure (5-4): CO_2 laser pulse, Pyro electric detector.

Photon Drag Detector: Opticon Corp Ltd., Model 7425

This detector was used exclusively as a timing monitor for the CO_2 laser, hence, a sensitivity calibration was unnecessary. A typical trace is shown below.

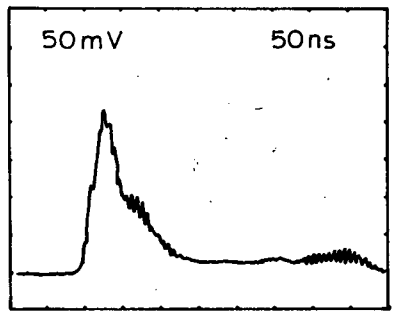

Figure (5-5): CO_2 laser pulse, Photon Drag Detector. Note the beating of longitudinal laser modes.

Gen Tech Energy Meter: Gen Tech Inc. Model LED-200-C

Fast ballistic energy meter, 5 msec response time.

Calibrated sensitivity at 10.6 μm is 7.8 $\frac{mV}{mJ}$

A typical trace is shown below.

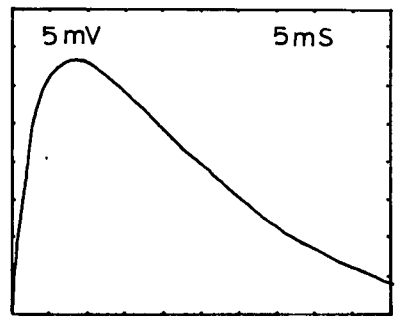

Figure (5-6): Response of Gen Tech energy meter to CO_2 laser pulse.

Apollo Energy Meter: Apollo Lasers Inc., Model ACM-100

Range: 5 mJ to 2 kJ, digital readout.

(4) Salt Optics

All infrared transmitting optics consisted of KCL, all mirrors were aluminum-coated front surface mirrors.

The figure below shows the measured transmission of a 6 mm KCL salt window (as used with the Au Ge detector) and of a 12 mm KCL flat (thickness of the salt lense) as a function of wavelength.

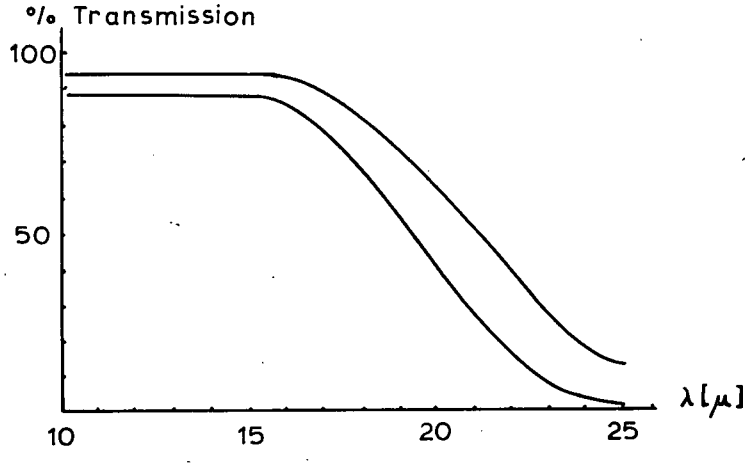

(5) Monochromator and Gratings

Monochromator: $\frac{1}{2}$ m Jerral Ash, 100 μm or 130 μm slits

Gratings: a) Yobin Ivon, 50 x 50 mm, 153 lines/mm

Blazed at 10.6 μm

Dispersion 110 Å/mm.

b) Bausch and Lomb, 2.7" x 2.7", 60 lines/mm

Blazed at 16 μm

Dispersion 300 Å/mm

(6) Optical Multichannel Analyser

Supplied by Princeton Applied Research Corp, Princeton N.J. The OMA used for the experiments described in Chapter IV was type 1205I. As this device is of considerable complexity, it will not be treated further in this appendix. For further information refer to the instruction manual, available from P.A.R. corp.

(7) Oscilloscopes

Tektronix 7704 with vertical amps 7A16 and 7A12

Tektronix 466 fast storage oscilloscope.

References

1. Lubin, M., Goldman, E., Soures, J., Goldman, L., Friedman, W., Letzring, S., Albritton, J., Koch, P., Jaakobi, B., Plasma Physics and Controlled Thermonuclear Fusion Research, Vol. 2, IAEA, Vienna, 1975.

2. Nuckolls, J.H.; Brueckner, K.A.; Kidder, R.E.; Kaliski, S.; Soures, J., Goldman, L.M., Lubin, M., Laser Interaction and Related Plasma Phenomena, Vol. 3B, ed. H.J. Schwarz and H. Hora, Plenum, N.Y., 1974.

3. Mead, W.C., Haas, R.A., Kruer, W.L., Phillion, D.W., Kornblum, H.N., Lindl, J.O., MacQuigg, D.R., Rupert, V.C., Phys. Rev. Lett. 37, 489 (1976).

4. Liu, C.S., Rosenbluth, M.N., White, R.B.; Biskamp, D., Weber, H.; Kruer, W., Valeo, E., Estabrook, K., Thomson, J.J., Langdon, B., Lasinski, B., Plasma Physics and Controlled Thermonuclear Fusion Research, Vol. 2, IAEA, Vienna, 1975.

5. Workshop on linear magnetic confinement, Seattle, Washington, 1977. Hosted by Mathematical Sciences Northwest, 2755 Northrup Way, Bellevue, Washington.

6. Dawson, J., Oberman, C., Phys. Fluids 5, 517 (1962).

7. Offenberger, A.A., Cervenan, H.R., Pasternak, A.W., J. Appl. Phys. 47, 1451 (1976).

8. Rutkowski, H., Scudder, D., Pietrzyk, Z., Appl. Phys. Lett. 26, 421 (1975).

9. Meyer, J., Albrecht, G.F., Hilko, B., Phys. Lett. 65A, 119 (1978).

10. Du Bois, D.F., Goldmann, M.V., Phys. Rev. Lett. 14, 544 (1965).

11. Drake, J.F., Kaw, P.K., Lee, Y.C., Schmidt, G., Phys. Fluids 17, 778 (1974).

12. Forslund, D., Kindel, J.M., and Lindman, E.L., Phys. Fluids 18, 1002 (1975).

13. Nishikawa, K., Phys. Soc. Jap. 24, 916 (1968).

14. Nishikawa, K., and Liu, C.S., Advances in Plasma Physics, Vol. 6, John Wiley and Sons, N.Y. 1976, p. 3 and p. 83, respectively.

15. Chen, F.F., Laser Interaction and Related Plasma Phenomena, Vol. 3A ed. Schwarz and Hora, Plenum, N.Y., 1974, p. 291.
This reference contains an excellent physical description of most parametric decay instabilities occuring in laser-plasma interaction.

16. Chen, F.F., Introduction to Plasma Physics, Plenum, N.Y. 1977.

17. Krall, N.A., Trivelpiece, A.W., Principles of Plasma Physics, McGraw-Hill, N.Y. 1973.

18. Boyd, T.J., Sanderson, J.J., Plasma Dynamics, Nelson, London, 1969.

19. Spitzer, L., Physics of Fully Ionized Gases, Intersc. Publ. N.Y., 1961.

20. Ripin, B.H., Young, F.C., Stamper, J.A., Armstrong, C.H., Decoste, R., McLean, E.A., Bodner, S.E., Phys. Rev. Lett. 39, 611 (1977) and references therein.

21. Schuss, J.J., Chu, T.K., Johnson, L.C., Phys. Rev. Lett. 40, 27 (1978).

22. Watt, R.G., Brooks, R.D., Pietrzyk, Z.A., Phys. Rev. Lett. 41, 170 (1978).

23. Baldis, H.A., Samson, J.C., Corkum, P.B., Phys. Rev. Lett. 41, 1719 (1978).

24. Kaw, P., Schmidt, G., Wilcox, T., Phys. Fluids 16, 1522 (1973).

25. Marlnic, M.E., Phys. Fluids 18, 837 (1975).

26. Hubert Houtman, Thesis, University of B.C., Sept. 1977.

27. Nicholson, Florence, Proc. Phys. Soc. A5, 506 (1971).

28. Steinhauer, L.C., Phys. Fluids 19, 1740 (1976).

29. Landau, L.D., Lifshitz, E.M., Vol. 5, Statistical Physics, Pergamon, Oxford, 1975.

30. Phillion, D.W., Kruer, W.L., Rupert, V.C., Phys. Rev. Lett. 39, 1529 (1977).

31. Grek, B., Pepin, H., Rheault, F., Phys. Rev. Lett. 38, 898 (1977).

32. White, M.S., Kilkenny, J.D., Dangor, A.E., Phys. Rev. Lett. 35, 524 (1975).

33. Lehmberg, R.H., Phys. Rev. Lett. 41, 863 (1978).

34. Donaldson, T.P., Hubbard, H., Spalding, I.J., Phys. Rev. Lett. 37, 1348 (1976).

35. Thomson, J.J., Max, C.E., Eastabrook, K., Phys. Rev. Lett. 35, 663 (1975).

36. Stamper, J.A., Papadopoulous, K., Dean, S.O., McClean, E.A., Bodner, S.E., Phys. Rev. Lett. 26, 1012 (1972).

37. Stamper, J.A., Ripin, B.H., Phys. Rev. Lett. 34, 138 (1975).

38. Lehmer, G., Pohl, F., Z. Physik 232, 405 (1970).

39. Jackson, J.D., Classical Electrodynamics, John Wiley & Sons, N.Y., 1975.

40. Albrecht, G.F., Källne, E., Meyer, J., Rev. Sci. Instr. 49, 1637 (1978).

41. Evans, D.E., Katzenstein, J., Rep. Prog. Phys. 32, 207 (1969).

42. Simpson, R.W., Talmi, Y., Rev. Sci. Instr. 48, 1295 (1977).

43. Griem, H., Plasma Spectroscopy, McGraw-Hill, N.Y., 1964.

44. Delcroix, A., Volonte, S., J. Phys. 13; Atom. Molec. Phys. 6, L4, (1973).

45. Drouet, H.G., Bolton, R., Phys. Rev. Lett. 36, 591 (1976).

46. Ng, A., Pitt, L., Sabriman, D., Offenberger, A.A., Phys. Rev. Lett. 42, 307 (1979).

47. Kruer, W.L., Valeo, E.J., Estabrook, K.G., Phys. Rev. Lett. 35, 1076 (1975).

48. Hagfors, T., J. Geophys. Res. 66, 1699 (1961).

49. Hallen, E., Electromagnetic Theory, John Wiley, N.Y., 1962.

50. Kupfermüller, K., Einfuhrung in die theorotische Elektrotechnik, Springer, Berlin, 1968.

51. Bekefi, G., Radiation Processes in Plasmas, John Wiley & Sons, N.Y., 1966.

52. Perratt, A.L., Phys. Fluids 18, 57 (1975).